



저작자표시-비영리-변경금지 2.0 대한민국

이용자는 아래의 조건을 따르는 경우에 한하여 자유롭게

- 이 저작물을 복제, 배포, 전송, 전시, 공연 및 방송할 수 있습니다.

다음과 같은 조건을 따라야 합니다:



저작자표시. 귀하는 원저작자를 표시하여야 합니다.



비영리. 귀하는 이 저작물을 영리 목적으로 이용할 수 없습니다.



변경금지. 귀하는 이 저작물을 개작, 변형 또는 가공할 수 없습니다.

- 귀하는, 이 저작물의 재이용이나 배포의 경우, 이 저작물에 적용된 이용허락조건을 명확하게 나타내어야 합니다.
- 저작권자로부터 별도의 허가를 받으면 이러한 조건들은 적용되지 않습니다.

저작권법에 따른 이용자의 권리는 위의 내용에 의하여 영향을 받지 않습니다.

이것은 [이용허락규약\(Legal Code\)](#)을 이해하기 쉽게 요약한 것입니다.

[Disclaimer](#)

Ph.D. Dissertation of Engineering

Polymer–Nanocomposite Based
Pressure Sensors and
Energy Harvesting Devices
for Wearable Applications

웨어러블 소자 응용을 위한
고분자 나노복합체 기반
압력센서와 에너지하베스팅소자 연구

February 2018

Department of Electrical and Computer Science
Collage of Engineering
Seoul National University

Bo–Yeon Lee

Polymer–Nanocomposite Based Pressure Sensors and Energy Harvesting Devices for Wearable Applications

지도 교수 이 신 두

이 논문을 공학박사 학위논문으로 제출함

2018년 2월

서울대학교 대학원
공과대학 전기·컴퓨터공학부

이 보 연

이보연의 공학박사 학위논문을 인준함

2017년 12월

위원장	<u>이 창 희</u>	(인)
부위원장	<u>이 신 두</u>	(인)
위원	<u>홍 용 택</u>	(인)
위원	<u>김 민 회</u>	(인)
위원	<u>나 준 희</u>	(인)

Abstract

Recently, wearable devices have been highlighted with the development of portable electronic devices and internet of things technologies. Unlike typical electronics, wearable devices need to form conformal and intimate contact with human and should be comfortable to wear or carry. Therefore, these devices must be thin, lightweight and flexible or stretchable. Furthermore, for the true commercialization of wearable electronics, it is essential to implement sensing technologies that enable friendly interaction with the user and develop a new power supply that can solve the problem of the use time and the volume from the existing battery. This thesis primarily aims to demonstrate the pressure sensors and energy harvesting devices suitable for advanced wearable electronics. It consists of two major categories, one of which is a flexible pressure sensor with high sensitivity, and other is a highly efficient, transparent and flexible energy harvesting device.

First, pressure sensors that can measure the strength of the contact have attracted much attention due to their great potential applications from touch panel to health monitoring systems. Especially, the sensitivity of pressure sensors is one of the most important performance factors for better emulating human skin and

more precisely capturing human motions. However, existing researches have limitation of the low sensitivity or the complex and costly fabrication process. In this thesis, a low-cost flexible pressure sensor based on the porous elastomer film contributing to the high sensitivity is developed. The elastomer film embedding uniformly dispersed micro-pores is found to have the low elastic modulus and the high deformability. A pressure sensor based on a porous elastomer film exhibits the high sensitivity in the low pressure region and the fast response.

Second, energy harvesting systems have emerged as a prominent research area and continue to grow at rapid pace due to the capability of replacing or supplementing a battery. Among them, triboelectric nanogenerators (TENGs) converting mechanical energy sources from surroundings into electricity have been extensively investigated due to the numerous advantages such as the cost-effectiveness, the fabrication simplicity, the robustness, the small volume, and the high efficiency. However, in the conventional TENGs, it was difficult to implement a flexible device because of metal layers. Although the researches replacing metals to flexible electrodes have been proposed, they have the limitation of a low output power. In this thesis, the research on the performance improvement of a transparent and flexible TENG through the conducting polymer and silver nanowires composite layer is described. A conducting polymer layer with high electronegativity contributes to the improvement of output power of TENG. And its characteristics of high transparency

and flexibility will make it suitable for advanced wearable applications. Furthermore, the increase of the conductivity and the surface roughness through the introduction of silver nanowires is found to further improve the output performance of TENG. The proposed TENG exhibits the highest output performance among the conventional transparent and flexible TENGs.

In summary, this thesis focuses on the performance improvement of pressure sensors and TENGs, which are core technologies of advanced wearable applications, through the utilization of polymer–nanocomposites such as the porous elastomer film and the nano–structured conducting polymer. The proposed approaches will provide a viable and effective framework for developing advanced wearable applications such as self–powered pressure sensor with human–friendly interactions.

Keyword: Wearable electronics, Polymer–nanocomposites, Elastomer, Flexible sensors, Capacitive pressure sensors, Triboelectric nanogenerators

Student Number: 2012–20834

Table of Contents

Abstract	i
Table of Contents	iv
List of Figures	vii
List of Tables.....	xiii
Chapter 1 Introduction.....	1
1.1 Wearable Electronics	1
1.2 Mechanical Sensors (Pressure Sensors)	4
1.3 Energy Harvesting Devices	7
1.4 Outline of Thesis	9
Chapter 2 Research Background.....	11
2.1 Functional Polymers.....	11
2.1.1 Conducting polymers	12
2.1.2 UV–curable polymers	15
2.1.3 Fluoropolymers	16
2.1.4 Biocompatible elastomers.....	17
2.2 Capacitive Pressure Sensor	19

2.2.1 Key parameters.....	19
2.2.2 Improving sensitivity of pressure sensors	21
2.3 Triboelectric Nanogenerator	26
2.3.1 Basic principle	26
2.3.2 Fundamental theory	28
Chapter 3 Highly Flexible Pressure Sensor	32
3.1 Introduction.....	32
3.2 Experimental Details	35
3.2.1 Fabrication of porous elastomer films.....	35
3.2.2 Fabrication of pressure sensors	37
3.2.3 Measurements of porous PDMS films and pressure sensors	38
3.3 Results and Discussion.....	39
3.3.1 Characteristics of porous PDMS films	39
3.3.2 Performance of single cell–type of pressure sensor	44
3.2.3 Performance of flexible array of pressure sensors	52
3.4 Summary	55
Chapter 4 Highly Efficient, Flexible, and Transparent Triboelectric Nanogenerator.....	56
4.1 Introduction.....	56
4.2 Experimental Details	61
4.2.1 Materials and sample preparation.....	61

4.2.2 Measurement and characterization.....	62
4.3 Triboelectric Property of PEDOT:PSS	64
4.4 Effect of AgNWs on Output of TENG	67
4.4.1 Surface roughness	67
4.4.2 Sheet resistance.....	69
4.5 Characteristics of PEDOT:PSS/AgNW Film.....	70
4.6 Output Performance of FT-TENGs.....	72
4.7 Practical Application of FT-TENGs.....	75
4.8 Summary	79
Chapter 5 Concluding Remark	80
Appendix (acronyms).....	82
Bibliography	83
Publications.....	93
국문초록	97

List of Figures

Figure 1.1 Diagram of flexible tactile sensors and wearable applications. (Ref. [1])	2
Figure 1.2 Power consumption spectrum for commercialized wearable electronics. (Ref. [2])	3
Figure 1.3 Schematic illustrations of three typical pressure sensing mechanism: (a) piezoelectric (b) piezoresistive, (c) capacitance (Ref. [3])	5
Figure 2.1 Chemical structures of the various conducting polymers (Ref. [6])	12
Figure 2.2 Chemical structure of PEDOT:PSS. The “dot” and “plus” represent the unpaired electron and positive charge on the PEDOT chain, respectively (Ref. [7])	14
Figure 2.3 Schematic illustration for the polymerization of photopolymer by UV light (Ref.: Wikipedia)	15
Figure 2.4 The chemical structure of PDMS (Ref.: Wikipedia)	18
Figure 2.5 Schematic illustration showing the working principle of a capacitive pressure sensor.	20
Figure 2.6 Examples of flexible pressure sensors based on (a) a bulk elastomer (Ref. [14, 15] and (b) an air gap as dielectric layer (Ref. [17, 18])	22

Figure 2.7 Cross-sectional image of polyolefin foam showing non-uniformity of the pore size (Ref. [4]).....	23
Figure 2.8 SEM images of structured PDMS: (a) micro-pyramids and (b) nano-needles (Ref. [19]).....	24
Figure 2.9 (a) Triboelectric series for common materials. (b) Schematic of operating mechanism for TENG in a short-circuit system (Ref. [2]).....	26
Figure 2.10 Theoretical models for (a) dielectric-to-dielectric contact-mode TENG and (b) conductor-to-dielectric contact-mode TENG (Ref. [23]).....	28
Figure 3.1 Fabrication process of an elastomer film with well-distributed micro-pores.....	35
Figure 3.2 The SEM images of six different porous PDMS films prepared from the mixtures of the PDMS and water with the weight ratio of water (c_w) ranging from 0.05 to 0.3. The white scale bars represent 10 μm	39
Figure 3.3 Porosity of the fabricated PDMS films as a function of c_w	40
Figure 3.4 (a) The cross-sectional image of a portion of the porous PDMS film with $c_w = 0.3$, observed with the SEM. The scale bar represents 100 μm . (b) Histogram of the diameter distribution of pores obtained from (a).	41
Figure 3.5 The SEM images of the porous PDMS film with various thickness.	41
Figure 3.6 Photographic images of the six PDMS films showing the dependence of the transparency on c_w under ambient light.	

The rectangular region enclosed by red dashed line in each sample represents the region of the porous PDMS film. A transparent sheet with three types of characters (Korean letters and block alphabets together with small alphabets in English) was placed between an illuminating light source and the PDMS film. The black scale bar is 1 cm. The size of the PDMS region is $1.5 \times 2 \text{ cm}^2$ 42

Figure 3.7 The dependence of the transmittance of the PDMS films on c_w from 0 to 0.3 in the visible range..... 43

Figure 3.8 The relative capacitance change (ΔC) to the initial capacitance under no pressure (C_0) as a function of the applied pressure. Note that for each c_w , three different samples were used for the measurements. The error was within 8.5 %. 45

Figure 3.9 The sensitivity ($S_{0,1}$) in the low pressure range from 0 to 0.1 kPa as a function of c_w 46

Figure 3.10 The values of the pressure–dependent sensitivity S of our sensors with different PDMS films as a function of the applied pressure. 47

Figure 3.11 The dynamic responses of two pressure sensors, fabricated using the porous PDMS films with $c_w = 0.0$ (black) and 0.3 (red), under the pressure of 0.2, 0.4, and 0.6 kPa for 10 s each. 50

Figure 3.12 The temporal response of the pressure sensor for $c_w = 0.3$ to consecutive taps..... 51

Figure 3.13. (a) A schematic diagram and (b) a photographic image of our 5×5 array ($3.3 \times 3.3 \text{ cm}^2$ in size) of flexible pressure sensors based on the porous PDMS film with $c_w = 0.3$

between two ITO-coated flexible PET substrates.....	52
Figure 3.14 The distribution of the capacitance change in the sensor array upon placing a weight of glass ($7\times 7\text{ mm}^2$, 0.02 kPa) in the rectangular region enclosed by the yellow dotted line. The gray level in the bar scale represents the magnitude of the relative capacitance change.	53
Figure 4.1 Various applications for flexible and transparent energy harvesting devices.....	57
Figure 4.2 Previous work of PEDOT:PSS-based TENGs (Ref. [86–66]).	58
Figure 4.3 Schematics showing (a) a metal–polymer combination of the conventional TENG, (b) a proposed design composed of a conducting polymer and silver nanowires for FT–TENG.....	59
Figure 4.4 Experimental setup of the SKPM measurement by AFM.	63
Figure 4.5 (a) SKPM images and (b) histogram distributions of contact potential difference (CPD) for the tribo–materials obtained from AFM measurements. The scale bars indicate 1 μm	64
Figure 4.6 (a) The schematic illustration and (b) the output voltage of the basic TENGs based on five–triboelectric materials.	65
Figure 4.7 (a) AFM 3D topographic images of PEDOT:PSS, AgNW and PEDOT:PSS/AgNW surfaces. (b) Line scan profiles corresponding to the red dashed lines in (a).....	68

Figure 4.8 Sheet resistance for ITO, PEDOT:PSS and PEDOT:PSS/AgNW films.	69
Figure 4.9 (a) Normalized resistance over the bending radius and (b) transmission over the wavelengths 380–780 nm for ITO on PEN (black) and PEDOT:PSS/AgNW on PDMS (red).....	70
Figure 4.10 Photographic image of PEDOT:PSS/ AgNW/PDMS film on a curved skin surface.	71
Figure 4.11 The output voltage of the TENG based on (a) PEDOT:PSS and (b) PEDOT:PSS/AgNW layers.	72
Figure 4.12 (a) The output voltage, the current and (b) the instantaneous power output of the optimized TENG depending on the external load resistance.....	73
Figure 4.13 Applications of the optimized TENG generated from gentle touch. (a) Photographic images and (b) output voltage of the FT–TENG. The rectangular region enclosed by orange dashed line and the circular region enclosed by yellow dashed line represent PEDOT:PSS/AgNW/PDMS film and PUA/PEDOT:PSS/AgNW/PDMS film, respectively.	76
Figure 4.14 Applications of the optimized TENG generated from various steps. (a) Photographic images and (b) output voltage of the FT–TENG. The rectangular region enclosed by orange dashed line and the circular region enclosed by yellow dashed line represent PEDOT:PSS/AgNW/PDMS film and PUA/PEDOT:PSS/AgNW/PDMS film, respectively.	77

List of Tables

Table 2.1 The physicochemical properties of EGC-1700 and DS-1000 series.	16
Table 3.1 The main characteristics of various capacitive-type pressure sensors.	49
Table 4.1 Summary of TF-TENGs	74

Chapter 1

Introduction

1.1 Wearable Electronics

A wearable electronic has emerged as a new form of electronics in a highly interactive way with the rapid development of technology based on IoT (Internet of things) and wireless sensor network. Numerous applications for wearable electronics range from portable infotainment* to health monitoring. The key technologies of wearable electronics can be divided into two categories, one of which is sensing technology, and the other is power system.

First, sensors capable of collecting information obtained from human body and surroundings are an important part of wearable electronics. Among various sensing technologies, mechanical sensors

* portable electronics that provide both of entertainment and information.

responsive to external mechanical deformations (e.g., pressure sensors) have attracted considerable attention due to their potential applications such as an electronic skin and health or motion monitoring systems as shown in Fig. 1.1 [1].

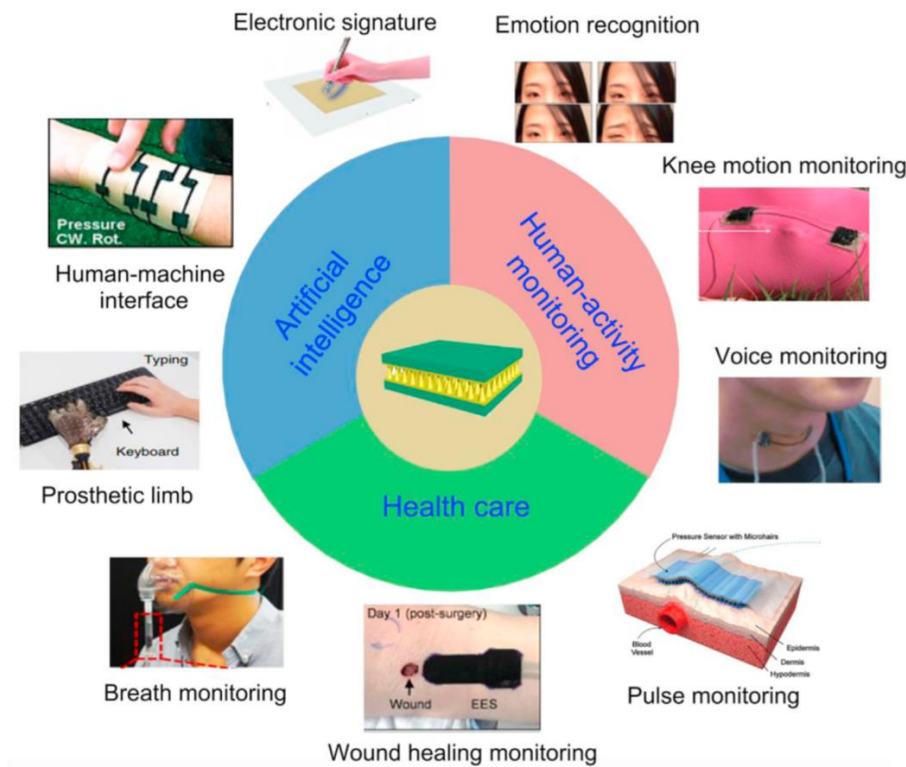


Figure 1.1 Diagram of flexible tactile sensors and wearable applications. (Ref. [1])

Second, wearable electronics require power ranging from several micro-watts to several tens of watts for operation as shown in Fig. 1.2 [2]. However, conventional power systems are limited in application of wearable electronics in that they are bulky and heavy with limited use time. From this perspective, sustainable energy

harvesting technologies utilizing solar, thermal, mechanical energy resources can be an ideal candidate as a new type of power sources to replace or supplement a battery.



Figure 1.2 Power consumption spectrum for commercialized wearable electronics. (Ref. [2])

Meanwhile, unlike typical electronics, wearable devices need to form conformal and intimate contact with objects to be monitored. Furthermore, they should be comfortable to wear or carry. Therefore, both of sensors and energy harvesting devices must be thin, lightweight and flexible or stretchable with high performance for true commercialization of wearable electronics.

1.2 Mechanical Sensors (Pressure Sensors)

Pressure and touch sensitivity is crucial for intuitive human-machine interfaces. The human's skin touch sensitivity is truly remarkable, and recreating the ability to sense force magnitudes in artificial systems could provide seamless interaction with robots or digital electronics. For example, current smartphone touchscreens and laptop trackpads can detect the position of fingers accurately, but cannot sense how much force users apply. Having such pressure information could enable more intuitive human-computer interactions such as pressure-gesture driven interfaces for future flexible or stretchable natural, wearable electronics. Even inside the human body, regular physiological activities generate various pressures, including blood pressure, intraocular pressure, etc., all of which are significant health indicators. For wearable electronics, having a flexible or stretchable pressure sensor on a device such as a watch can be useful for two reasons: (i) as pressure-based user input interfaces, and (ii) non-invasive monitoring of blood pressure if the sensor is sensitive enough to pick up pulsations from the radial artery. This prominent feature enables the successful application of pressure sensors in personal electronic devices, artificial intelligence and industrial production applications.

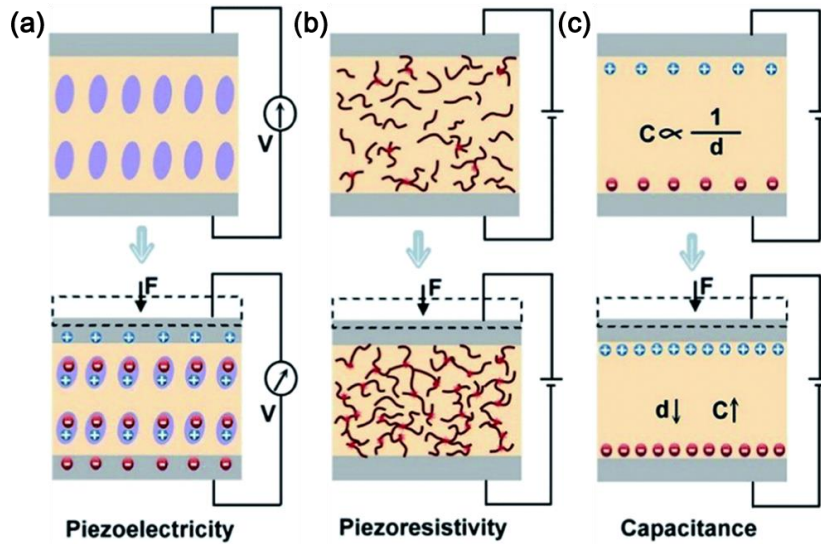


Figure 1.3 Schematic illustrations of three typical pressure sensing mechanism: (a) piezoelectric (b) piezoresistive, (c) capacitance (Ref. [3]).

There are several types of pressure sensing technologies such as piezoelectric, piezoresistive and capacitive as shown in Fig. 1.3 [3]. Each of these mechanisms has its own characteristics, the details of which are briefly described below. Piezoelectric pressure sensors use the electrical charges generated in certain types of solid materials (such as crystals and certain ceramics) in response to applied mechanical stresses (Fig. 1.3(a)). The occurrence of electric dipole moments in solids contributes to the piezoelectric effect. This technology is commonly employed for the measurement of highly dynamic pressures. In other words, piezoelectric sensors generate a

signal only if there is a variation in pressure, hence they fail to detect static loads. Static loads can be detected with resistive and capacitive sensor networks. Piezoresistive pressure sensors detect the change of electrical resistance as pressure deforms the sensing materials (Fig. 1.3(b)). Resistive sensors are generally suitable for use over large pressure ranges, making it possible for large strains to be reliably measured. Capacitive pressure sensors usually use a diaphragm and pressure cavity to create a variable capacitor to detect strain due to applied pressure, capacitance decreasing as pressure deforms the diaphragm (Fig. 1.3(c)). Among three types, a capacitive one can be a promising candidate for a pressure sensor in wearable electronics due to its higher accuracy, lower dependency on surroundings and less affection to the number of pressure cycles, over the other two types [4]. However, low sensitivity resulting from the relatively small change in the capacitance of parallel plates needs to be improved. The theoretical background of capacitive pressure sensors for the sensitivity improvement will be discussed in more detail in **Section 2.2**.

1.3 Energy Harvesting Devices

Energy harvesting systems have emerged as a prominent research area and continue to grow at rapid pace due to being capable of replacing or supplementing a battery. Among various technologies, energy harvesters which can convert electrical energy from vibrational and mechanical energy sources are very promising tools [5]. Because, mechanical energy is abundant in our living environment, though it is irregular energy with variable frequency and magnitude, such as airflow, noises, human activity.

The energy harvesting devices utilizing mechanical kinetic energy is typically categorized into two types: piezoelectric and triboelectric nanogenerators (TENG). Piezoelectric nanogenerators (PNGs) are based on the piezoelectric effect, in which an electric charge accumulates in certain materials in response to applied mechanical stress. Piezoelectric materials include crystals, ceramics, polymers, and proteins. However, PNGs still show either insufficient output performance when used to operate useful mW-level consumer electronics due to their low piezoelectric properties or size limitations.

On the other hand, TENG has been gaining strong attention during the last few years because of the very high reported power density ($1\text{--}10\text{ W/cm}^{-3}$), and the number of possible practical configurations. TENG is based on the triboelectric effect, in which a material becomes electrically charged when it comes into frictional

contact with another material. Once the two materials are charged, the displacement between two can generate an electric current through an electrode connecting them. Due to the novelty of this approach, a great deal of work is expected on geometry optimization, materials development and deposition techniques for dielectric coatings and thin film layers. The theoretical background of TENGs for the performance improvement will be discussed in more detail in **Section 2.3**.

1.4 Outline of Thesis

The thesis contains five chapters including **Introduction** and **Concluding Remark**. In **Chapter 1**, the overview and the challenges of wearable electronics are briefly introduced. **Chapter 2** explains the functional polymers used in this thesis and presents the theoretical background with regard to capacitive type of flexible pressure sensors and triboelectric nanogenerators. In **Chapter 3**, a low-cost flexible pressure sensor with high sensitivity in the low pressure range is demonstrated. An elastomer film with uniformly distributed micro-pores was used as the dielectric layer determining compressibility of devices. The dispersion of the micro-pores in the elastomer film results from the phase separation between a prepolymer material and an insoluble solvent to the elastomer, followed by the subsequent evaporation of the solvent within the polymer matrix after polymerization. The enhanced deformability by the pore structures leads to the improved sensitivity. The sensitivity was found to primarily vary with the porosity of the elastomer film. In **Chapter 4**, a highly efficient, flexible and transparent TENG using the nano-structured conducting layer having high tribo-negativity is demonstrated. For the first time, the conducting polymer, poly(3,4-ethylenedioxythiophene):poly(styrene sulfonate) (PEDOT:PSS), was found to have a high tendency to attract electrons during contact. Moreover, the increase of the contact area resulting from the silver nanowires placed beneath the PEDOT:PSS layer further enhanced the output performance. The proposed FT-TENG built on a

stretchable substrate exhibits a high transparency and the excellent output performance on a random surface like a skin or a fabric. Finally, **Chapter 5** provides summary and concluding remarks.

Chapter 2

Research Background

2.1 Functional Polymers

Polymeric materials offer far greater design flexibility and processing simplicity than current inorganic materials. Moreover, a significant advantage of them concerns the ability to combine various functional groups and fragments, as well as to form stable films that can be readily applied onto various substrates through simple methods such as spin coating. In this thesis, these polymers with advanced optic and/or electronic properties as well as ease of processing are utilized to contribute to the performance improvement of wearable devices. Therefore, the characteristics of the functional polymers such as conducting polymers, photocurable polymers, fluoropolymers and biocompatible elastomers will be described in this section 2.1.

2.1.1 Conducting polymers

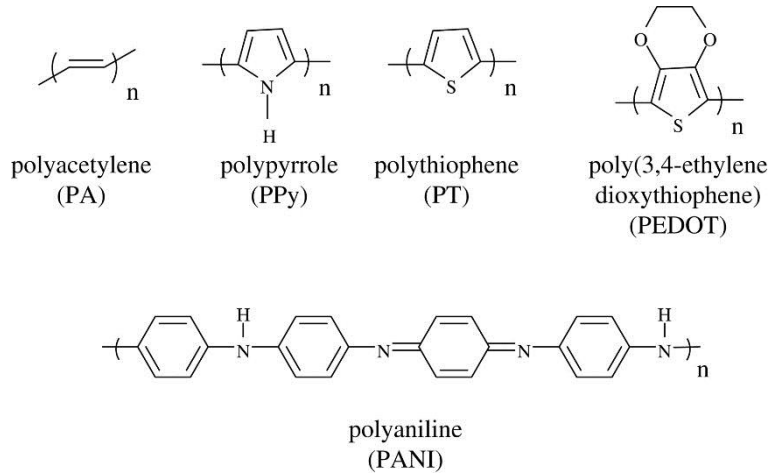


Figure 2.1 Chemical structures of the various conducting polymers (Ref. [6]).

Conducting polymers (CPs) are a special class of polymeric materials with electronic and ionic conductivity [6]. CPs have backbones of contiguous sp^2 hybridized carbon centers. One valence electron on each center resides in a p_z orbital, which is orthogonal to the other three sigma-bonds. All the p_z orbitals combine with each other to a molecule wide delocalized set of orbitals. The electrons in these delocalized orbitals have high mobility when the material is "doped" by oxidation, which removes some of these delocalized electrons. Thus, the conjugated p -orbitals form a one-dimensional electronic band, and the electrons within this band become mobile when it is partially emptied. Due to the presence of a conjugated π -

electron backbone, these polymers exhibit electronic properties such as low energy optical transmission, low ionization potential and high electron affinities. The electrical properties can be fine-tuned using the methods of organic synthesis and by advanced dispersion techniques. These unique properties make these materials suitable for numerous applications such as thin film transistors, organic light emitting diodes, sensors, supercapacitors, organic solar cells and electrochromic displays. The structures of the widely used CPs are depicted in Fig. 2.1 [6].

Among several conducting polymers, poly(3,4-ethylenedioxythiophene) (PEDOT) has attracted a great deal of interest due to its enormous advantages such as high conductivity, high electrochemical and thermal stability, and optical transparency. Generally, this polymer that is insoluble becomes water-soluble in combination with polystyrene sulfonic acid (PSS) as shown in Fig. 2.2 [7]. The use of PEDOT:PSS ranges from antistatic coating applications (cathode ray tube screens, electronic packaging, photographic films, LCD polarizers), electronic and optoelectronic applications (all organic field effect transistors, organic light emitting diodes, capacitors, photovoltaic, photodetectors), sensors.

The conductivity of PEDOT:PSS can be significantly improved by a post-treatment with various compounds, such as ethylene glycol, dimethyl sulfoxide and amphiphilic fluoro-compounds. This conductivity is comparable to that of representative transparent electrode materials, indium-tin-oxide (ITO), and it can be further improved after a network of carbon nanotubes and silver nanowires

(AgNWs) is embedded into PEDOT:PSS [8] and used for flexible organic devices [9].

In this thesis, PEDOT:PSS is usually used as a highly flexible and transparent electrode materials. Particularly, the effect of the conductivity and the surface roughness resulting from AgNWs beneath a PEDOT:PSS layer on the output performance of a TENG will be discussed in **Chapter 4**.

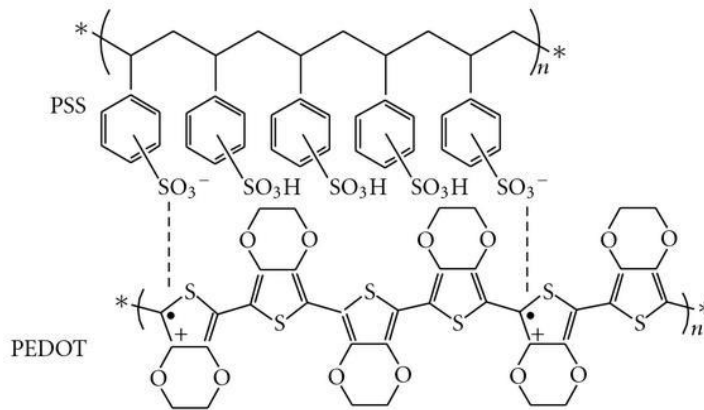


Figure 2.2 Chemical structure of PEDOT:PSS. The “dot” and “plus” represent the unpaired electron and positive charge on the PEDOT chain, respectively (Ref. [7]).

2.1.2 UV-curable polymers

A photopolymer or light-activated resin is a polymer that changes its properties when exposed to light, often in the ultraviolet or visible region of the electromagnetic spectrum [10]. Among them, ultra violet (UV)-curable polymers (as shown in Fig. 2.3.) have the major advantage of a short-processing time by UV-exposure ($\lambda = 250 \sim 400 \text{ nm}$) in a few seconds or minutes. UV-curable polymers such as polyurethane acrylate (PUA) and polyethylene glycol acrylate have been mostly used in soft lithography [11]. Especially, since PUA has several notable characteristics such as high transparency, high chemical stability and adjustability of elastic modulus, it has been successfully utilized, ranging from a soft mold [12] to a transparent and flexible substrate [13].

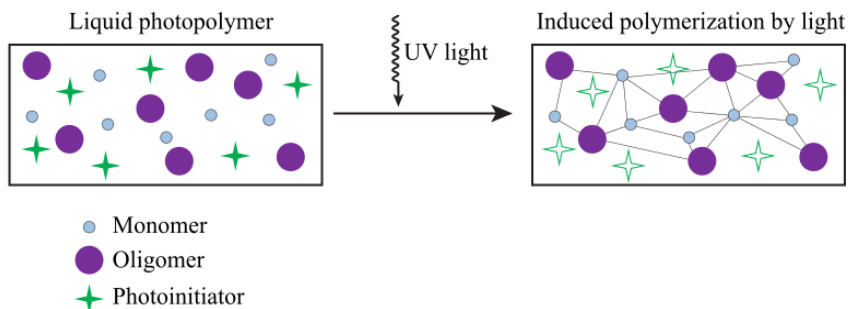


Figure 2.3 Schematic illustration for the polymerization of photopolymer by UV light (Ref.: Wikipedia).

2.1.3 Fluoropolymers

A fluoropolymer is a fluorocarbon-based polymer with multiple strong carbon-fluorine bonds. It is characterized by a high resistance to solvents, acids, and bases. Fluorous-solvents are very highly fluorinated liquids, which are highly environmentally friendly, non-flammable and rarely toxic to humans. Moreover, one of characteristics that can play an important role in microelectronics is low surface tension resulting from the C-F bond of the fluorinated surface. Commercially available fluoropolymers include EGC-1700 (3MTM Novec) and DS-1120F (Harves Co., Ltd.). Table 2.1 describes the physicochemical properties of EGC-1700 and DS-1120F obtained from the data sheet.

Table 2.1 The physicochemical properties of EGC-1700 and DS-1000 series.

Property	EGC-1700	DS-1000 series
Appearance	clear, colorless or light-colored	clear, colorless or light-colored, slight ether odor
Surface tension	11 ~ 12 dynes/cm	11 ~ 12 dynes
Dielectric constant	3.1 @ 1kHz	2.1 @ 1GHz
Boiling point	61° C	80° C

The thickness of these films can be uniformly controlled by simply varying the solution coating speed and the solution concentration. In **Chapter 3**, these fluoropolymers are used for easy separation between materials without any mechanical and chemical damages owing to the strong hydrophobic nature of them.

2.1.4 Biocompatible elastomers

An elastomer is a polymer with both viscosity and elasticity and very weak inter-molecular forces, generally having low Young's modulus and high failure strain compared with other materials. Each of the monomers which link to form the polymer is usually made of carbon, hydrogen, oxygen or silicon. Elastomers are amorphous polymers existing above their glass transition temperature, so that considerable segmental motion is possible. The most widely used elastomer in microfabrication is polydimethylsiloxane (PDMS) because it is highly elastic, crystal clear, inert, and non-flammable. PDMS is formed of an inorganic backbone of alternating silicon and oxygen atoms. Two methyl groups are attached to each silicon atom of the backbone chain as shown in Fig. 2.4. PDMS has a low surface energy (19.8 mN/m at 20° C), and the surface can be adjusted by exposure to UV light, ozone and plasma discharges.

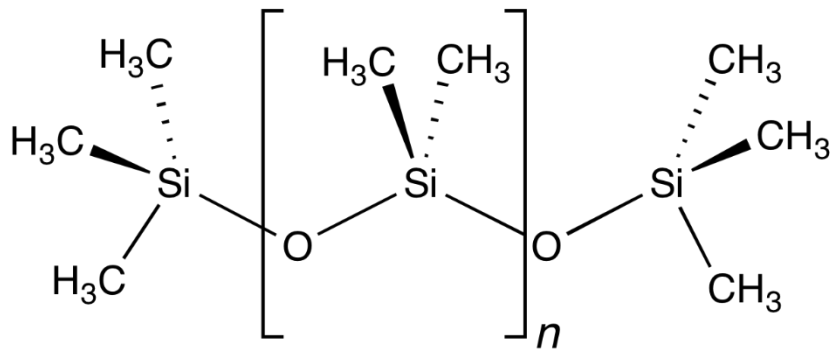


Figure 2.4 The chemical structure of PDMS (Ref.: Wikipedia).

PDMS also has a low polarity, and is chemically inert. Most aqueous solvents do not infiltrate or swell appreciably the silicon rubber. PDMS can be tuned to have an elastic modulus ranging from 0.1 to 3.5 MPa by altering its curing temperature, the ratio of applied curing agent to base. In the thesis, PDMS films are used as the dielectric layer of pressure sensors (**Chapter 3**) and the transparent and stretchable substrates (**Chapter 4**).

2.2 Capacitive Pressure Sensor

Although the conventional silicon-based pressure sensors have high sensitivity, it is challenging to adapt it for flexible and wearable electronics due to brittleness of silicon. Therefore, flexible polymers such as elastomers have been used in recent years as the dielectric layer of pressure sensors. In this section, the key parameters determining the sensitivity of capacitive flexible pressure sensors and methods for improving sensitivity will be described.

2.2.1 Key parameters

In a commonly used parallel plate capacitor, capacitance is given by the equation

$$C = \epsilon_0 \epsilon_r A / d, \quad (2.1)$$

where C is the capacitance, ϵ_r is the relative dielectric constant of the dielectric layer between the electrodes, ϵ_0 is the permittivity of free space, A is the area of overlap of the two electrodes in square meters, and d is the distance between the electrodes in meters (or thickness of the dielectric layer), ignoring fringe electric fields. An applied pressure causes the device to deflect and the capacitance to change as shown in Fig. 2.5. The pressure sensitivity S can be defined as

$$S = \delta (\Delta C / C_0) / \delta P, \quad (2.2)$$

where P denotes the applied pressure, and C and C_0 denote the capacitances with and without applied pressure, respectively. According to the eq. (2.2), the sensitivity is determined by how much capacitance changes under the applied pressure P . The capacitance change relies on the compressibility of the dielectric layer that is in contact with the force applied. In other words, in order for high sensor sensitivity, which is required for good signal to noise ratios, it is important that the mechanical compressibility of the dielectric material is large so that a small applied force can decrease d significantly.

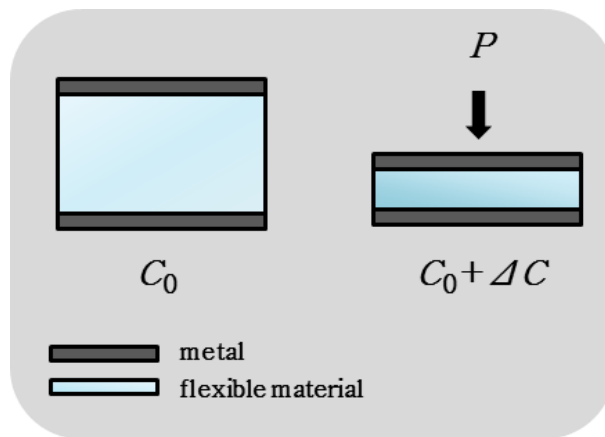


Figure 2.5 Schematic illustration showing the working principle of a capacitive pressure sensor.

The response time is also an important parameter in evaluating the performance of pressure-sensing devices, particularly those used in dynamic real-time sensing. The response time is defined as

the time consumption of a pressure sensor during response processes, from inputting pressure to producing a stable signal output. Both advances in instant-response displays and real-time monitoring health care systems require shortening of the response time, and devices with quick response capabilities (response time <100 ms) are required. The operating voltage, which is the voltage required to sustain regular operation of devices, is a critical factor in determining the power consumption. Decreasing the operating voltage and the corresponding power consumption is an indispensable trend of wearable electronic devices. It is worth noting that the parameters mentioned are inseparable in determining the overall performance of pressure sensors.

2.2.2 Improving sensitivity of pressure sensors

Equation (2.2) indicating the sensitivity of capacitive pressure sensor has three variables (ϵ_r , A , and d), and ϵ_0 is always constant, whereas d is easily changed by external forces. As mentioned earlier, the greater the compressibility of the material used, the greater the sensitivity of the sensor will be.

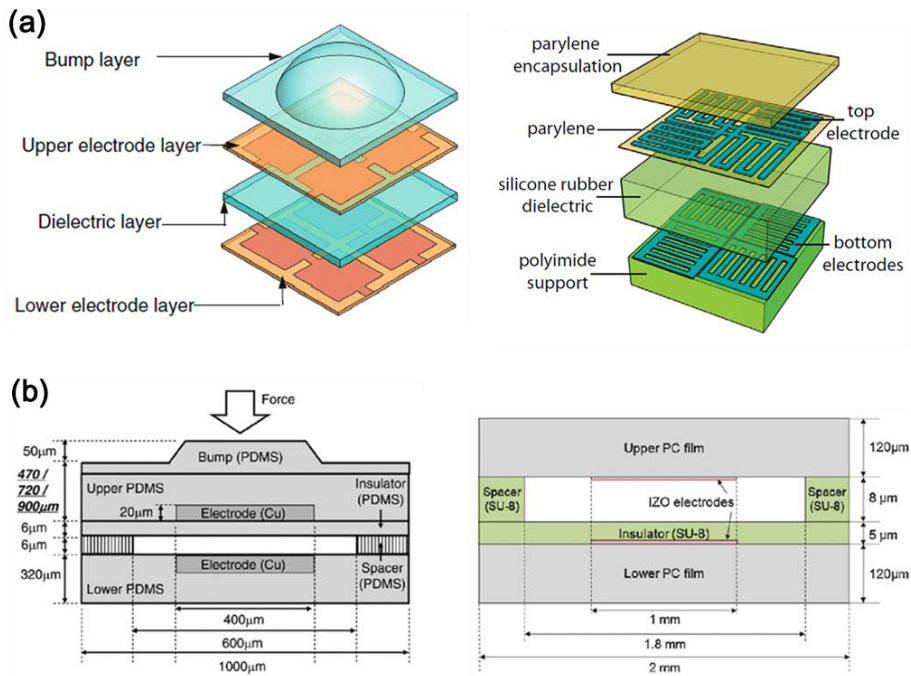


Figure 2.6 Examples of flexible pressure sensors based on (a) a bulk elastomer (Ref. [14, 15] and (b) an air gap as dielectric layer (Ref. [17, 18]).

In this regard, elastomers with fairly low viscoelasticity can be ideal materials for the dielectric layer of a capacitive pressure sensor. Furthermore, elastomers are inherently flexible and therefore suitable for use in flexible electronic devices. One of the most straightforward methods of making an elastomeric pressure sensor is to directly use the bulk elastomer as the dielectric materials sandwiched between two electrodes as shown in Fig. 2.6(a) [14–16]. When the elastomer is compressed, the capacitance of the sensor will change and this can be measured. Instead of using an elastomer as

dielectric, air gap can be also used with elastomeric membranes as shown in Fig. 2.6(b) [17, 18]. As pressure is applied to the membrane, the distance between the electrodes decreases, and thus the capacitance increases. The fabrication of such these configurations is reasonably straightforward; however, the sensitivity of these sensors is fairly low. It is difficult to detect stimuli in the low pressure range.

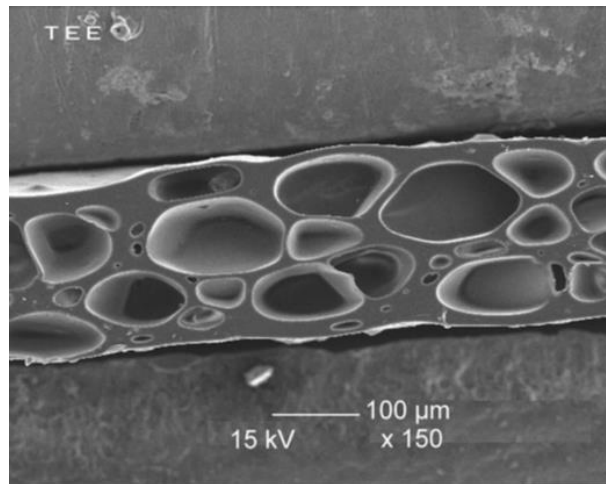


Figure 2.7 Cross-sectional image of polyolefin foam showing non-uniformity of the pore size (Ref. [4]).

Although polyolefin foams containing entrapped gaseous bubbles as shown in Fig. 2.7 were used as a compressible dielectric material [4], elastomers with a low mechanical modulus such as PDMS need to be used for high mechanical sensitivity.

Therefore, the introduction of micro-/nano-structures on the surface of a PDMS film was suggested to develop highly flexible pressure sensor even in the low pressure regime [19]. Fig. 2.8 shows the scanning electron microscopy (SEM) images of proposed micro-/nano-structured PDMS. These micro-/nano-structures have a similar effect with the addition of air gaps in an orderly fashion within the elastomer layer. The sensors with the structured films exhibit high sensitivity even in the low pressure range. The dramatic increase in sensitivity of the structured films over the unstructured films can be attributed to two main factors: (1) there is far less elastic resistance in the structured films because of the air voids in the PDMS film, and (2) when the structured films are compressed the displaced volume is air, which has a lower dielectric constant ($\epsilon_r=1.0$) than PDMS ($\epsilon_r\sim 3.0$). Therefore, the increase in capacitance in the structured film arises from the reduction in the distance between the two electrode plates, and is enhanced further by the increase in effective dielectric constant.

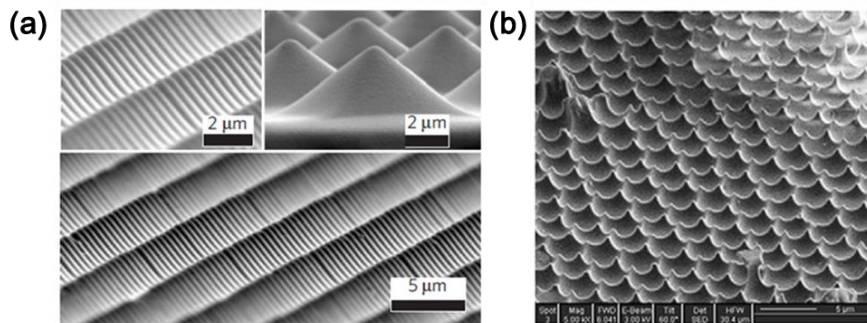


Figure 2.8 SEM images of structured PDMS: (a) micro-pyramids and (b) nano-needles (Ref. [19]).

However, the fabrication process includes vacuum-based process so that they generally require complex and expensive fabrication processes. To overcome these limitations, in **Chapter 3**, a simple and cost-effective approach to construction of flexible pressure sensor with high sensitivity in low-pressure range will be discussed.

2.3 Triboelectric Nanogenerator

2.3.1 Basic principle

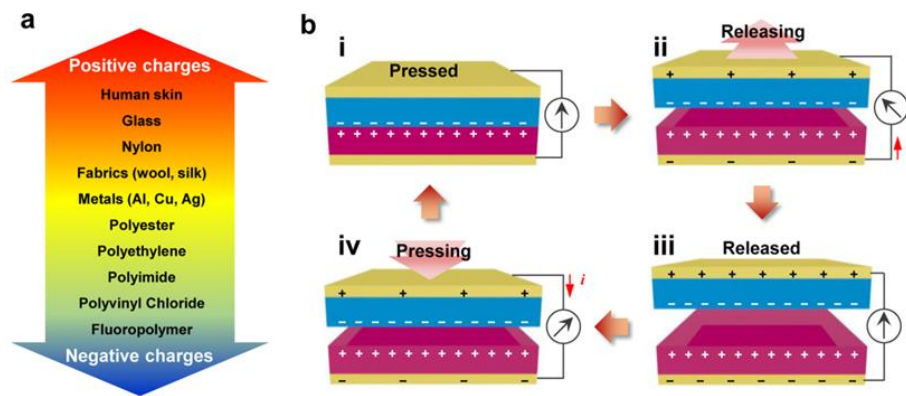


Figure 2.9 (a) Triboelectric series for common materials. (b) Schematic of operating mechanism for TENG in a short-circuit system (Ref. [2]).

The operating principle of TENG with the basic mode of vertical contact-separation mode can be described by the coupling of contact electrification and electrostatic induction [20]. Although the exact mechanism of contact electrification is still under dispute, the triboelectric charges are believed to be due to the charge (electrons, ions, or both) transfer when two materials come into contact and separate [21, 22]. A triboelectric series as shown in Fig. 2.9(a) refers to an empirically determined list of materials' tendencies to acquire positive or negative charges on the surface when they go through contact electrifications [21]. The farther the two materials

are in the triboelectric series, the more charge can be obtained. The working mechanism of TENGs is illustrated in Fig. 2.9(b). When two materials with different triboelectric polarities are brought into contact with each other (inset i in Fig. 2.9(b)), the triboelectric effects promote charge transfer between the two surfaces, resulting in the formation of opposite charges on each side of the surface. When the two surfaces are separated (inset ii in Fig. 2.9(b)), compensating charges are built up on the top and bottom electrodes due to electrostatic induction. Note that it is reasonable to assume that the tribo-charges are uniformly distributed at the two surfaces with negligible decay. This induction promotes current flow from the positive to the negative sides of the materials through the external circuit until the accumulated charges are neutralized and balanced on all sides of the electrodes (inset iii in Fig. 2.9(b)). Similarly, as the two different charged materials are brought closer to each other, the current flows from the negative to positive sides of the materials (inset iv in Fig. 2.9(b)). Consequently, the cyclic contact and separation between the two materials drive the output current flow back and forth between the positive and negative electrodes.

2.3.2 Fundamental theory

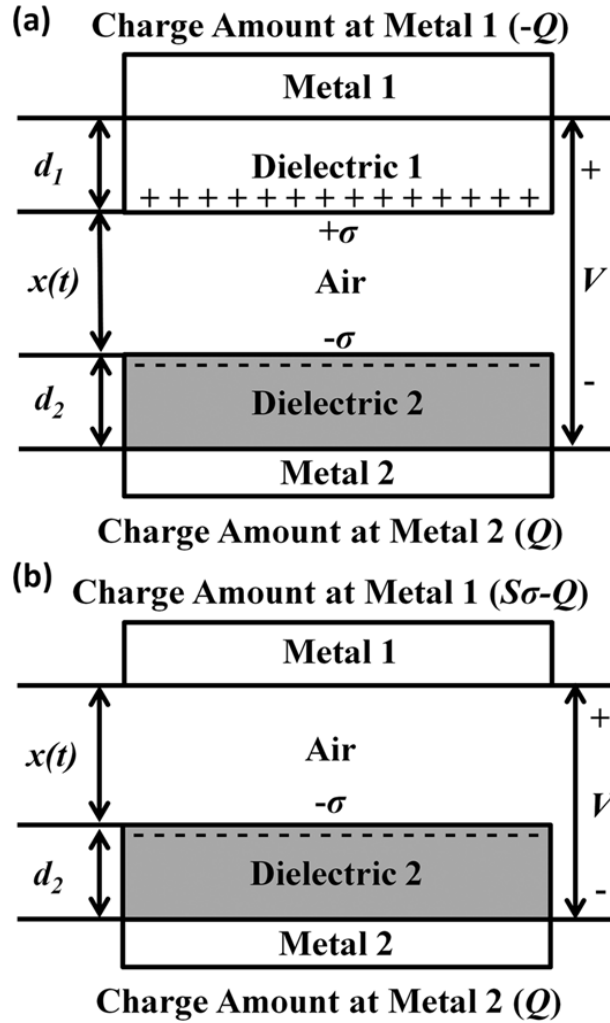


Figure 2.10 Theoretical models for (a) dielectric-to-dielectric contact-mode TENG and (b) conductor-to-dielectric contact-mode TENG (Ref. [23]).

The basic structure for contact–separation TENG is shown in Fig. 2.10 [23]. Based on the materials for the triboelectric pairs, the contact–separation TENG is mainly divided into two categories: dielectric–to–dielectric and conductor–to–dielectric types. The model built for a dielectric–to–dielectric contact mode TENG is shown in Fig. 2.10(a).

The most important theoretical equation for representing the real–time power generation of a TENG is a relationship among three parameters: the voltage (V) between the two electrodes, the amount of transferred charge (Q) in between, and the separation distance (x) between the two triboelectric charged layers, which can be named the V – Q – x relationship [24]. The two dielectric plates, with thicknesses of d_1 and d_2 and the relative dielectric constants ϵ_{r1} and ϵ_{r2} , respectively, are stacked face to face as two triboelectric layers. At the outer surface of these two dielectrics, two metal layers are deposited as two electrodes.

With the above model, the V – Q – x relationship of such a contact–mode TENG can be derived based on electrodynamics. Since the area size (S_{area}) of the metals is several orders of magnitude larger than their separation distance ($d_1 + d_2 + x$) in the experimental case, it is reasonable to assume that the two electrodes are infinitely large. Under this assumption, the charges on the metal electrodes will uniformly distribute on the inner surfaces of the two metals. Inside the dielectrics and the air gap, the electric field only has the component in the direction perpendicular to the surface, with the positive value pointing to Metal 2. From the Gauss theorem, the

electric field strength at each region is given by

$$\text{Inside dielectric 1: } E_1 = -Q/S \epsilon_0 \epsilon_{r1} \quad (2.3)$$

$$\text{Inside the air gap: } E_{\text{air}} = (-Q/S + \sigma(t)) / \epsilon_0 \quad (2.4)$$

$$\text{Inside dielectric 2: } E_2 = -Q/S \epsilon_0 \epsilon_{r2} \quad (2.5)$$

The voltage between the two electrodes can be given by

$$V = E_1 d_1 + E_2 d_2 + E_{\text{air}} x \quad (2.6)$$

Substituting Eq. (2.3)–(2.5) into Eq. (2.6), we can obtain the V - Q - x relationship for dielectric-to-dielectric TENG in contact-mode, which is given by

$$V = (-Q/S \epsilon_0) (d_1 / \epsilon_{r1} + d_2 / \epsilon_{r2} + x(t)) + \sigma x(t) / \epsilon_0 \quad (2.7)$$

Similarly, the model for the conductor-to-dielectric category is built, as shown in Fig. 2.10(b). In this structure, we no longer have Dielectric 1 and now Metal 1 plays two roles: both as the top triboelectric layer and as the top electrode. Therefore, the total charges in Metal 1 now have two parts: one is the triboelectric charges ($S\sigma$), the other is the transferred charges between the two electrodes ($-Q$). Thus, the total charges in Metal 1 are $(S\sigma - Q)$.

From a similar derivation, the V - Q - x relationship for this model is given by

$$V = E_2 d_2 + E_{\text{air}} x = (-Q/S \epsilon_0) (d_2 / \epsilon_{r2} + x(t)) + \sigma x(t) / \epsilon_0 \quad (2.8)$$

Eq. (2.8) is exactly the same equation as Eq. (2.7) if $d_1 = 0$. If we

define the effective thickness constant d_0 as $d_1/\epsilon_{r1}+d_2/\epsilon_{r2}$ for Eq. (2.6) and d_2/ϵ_{r2} for Eq. (2.8), the V - Q - x relationship for both these two types can be unified as the following equation.

$$V = (-Q/S\epsilon_0)(d_0+x(t)) + \sigma x(t)/\epsilon_0 \quad (2.9)$$

Chapter 3

Highly Flexible Pressure Sensor

3.1 Introduction

Pressure sensors have attracted much attention over the past few years due to their potential for various applications including object detection, haptic displays, and fingerprint sensors [4, 17, 25]. In recent years, much effort has been made toward improving the sensitivity of a flexible pressure sensor in the subtle-touch regime (1 Pa–1 kPa) as well as the low pressure range (1 kPa–10 kPa) since there is a tremendous demand for more accurate, delicate pressure sensing elements that can be implemented into health care and medical diagnosis systems [26–28] as well as electronic skin (e-skin) systems [16, 19, 29–31]. The pressure-sensing technology is typically categorized into three types: piezoelectric– [27, 32–38], piezoresistive– [29–31, 39–46] and capacitive–types [4, 14–19, 28, 47–51]. Among them, the capacitive-type has been

most widely studied owing to several advantages such as low dependence on temperature and humidity, low power consumption, and highly repeatable response, over the other two types [4, 51–53]. Basically, in the capacitive-type pressure sensor, the sensitivity depends primarily on how much the capacitance can be changed under applied pressure. The magnitude of the capacitance change is determined by the change in the dielectric constant, the thickness of a dielectric layer, or the surface area of an electrode. The thickness change of a dielectric layer is generally adopted. Moreover, an air gap [17, 18, 47] or a highly elastic material [14–16, 48–50] is often introduced to improve the physical properties of the dielectric layer. However, such simple modification of the device configuration limits the sensitivity in a low pressure region, meaning that it is applicable only for high pressure operations such as the object detection [4] and the plantar pressure measurement [14, 48]. Although several methods of introducing micro- or nano-structures on the surface of a thin dielectric layer, for example, micro-pyramids [19, 28] and nano-needles [51], have been suggested to solve the problem of the poor sensitivity in the low pressure regime, they generally require complex and expensive fabrication processes. This directly leads to the need of a simple and cost-effective approach to the construction of pressure sensors that have the high sensitivity in the low pressure range for skin-mimicking applications such as an e-skin.

In this chapter, we demonstrated a capacitive-type pressure sensor with the high sensitivity in the low pressure range using a porous elastomer film as a dielectric layer. Our porous film was

fabricated simply using a mixture of an elastomer material of siloxane polymers and water droplets without any additive such as an emulsifying agent. Due to the improved deformability of such elastomer dielectric layer with micro-pores, the sensitivity was greatly enhanced and the detectable range of pressure became significantly wide. Moreover, the sensitivity was found to easily vary with the porosity of the dielectric elastomer film through the mixing ratio of siloxane polymers and water. Our pressure sensor using the elastomer film showed the excellent sensitivity, the relatively fast response (< 150 ms), and potential for flexible touching and pressure-sensing applications.

3.2 Experimental Details

3.2.1 Fabrication of porous elastomer films

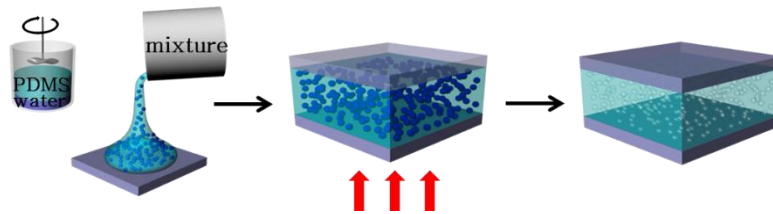


Figure 3.1 Fabrication process of an elastomer film with well-distributed micro-pores.

Figure 3.1 shows the fabrication process of our porous elastomer film used as a dielectric layer in a pressure sensor. Polydimethylsiloxane (PDMS; Sylgard 184, Dow Corning Corp.) was chosen as a base material owing to its high chemical and thermal stability together with the low elastic modulus, and deionized (DI) water was selected as a dispersion substance. Note that the boiling point of DI water is higher than the curing temperature of PDMS (70°C). A solution of the PDMS prepolymers, mixed with a curing agent at the weight ratio of 10:1, and water were first mechanically stirred in a container at the rate of 2600 rpm for 10 min. Through the stirring process, micro-droplets of DI water were uniformly dispersed in the PDMS solution due to the insolubility of water. The PDMS solution containing micro-droplets of water was then placed between two glass substrates that were treated to be hydrophobic by dip-coating in a solution of a chemically inert fluoropolymer (EGC-

1700, 3M) at the concentration of 2% in a hydrofluoroether solvent. The dipping speed was 80 mm/min. The gap between the two substrates was maintained using a tape spacer of about 100 μm -thick. Note that for the case of a hydrophilic substrate, no uniform dispersion of water droplets in the PDMS solution can be achieved because of the hydrophilic nature of water which results in strong interaction with the hydrophilic surface. The assembled sample was heated at the curing temperature of the PDMS prepolymer (70°C) for 24 h to achieve the thermal cross-linking of the PDMS and the evaporation of water confined in the PDMS. A fully polymerized PDMS film, having micro-pores where water was initially contained before evaporated, was produced as a porous, dielectric elastomer layer between the two substrates. The porous PDMS film was finally detached from the substrates without any mechanical damage owing to the strong hydrophobic nature of the fluoruous polymer (EGC 1700) used. It was used as a dielectric layer in our capacitive-type pressure sensor. Note that our porous PDMS film of about 100 μm -thick is very flexible and elastic so that it may be useful for other flexible device applications.

Depending on the weight ratio (c_w) of water mixed in the PDMS solution ($c_w = 0, 0.05, 0.1, 0.15, 0.2, 0.25, \text{ and } 0.3$ in our case), the transparency and the porosity of the PDMS film were adjusted. Above a critical value (about 0.5) of c_w , water and the PDMS solution were macroscopically phase-separated in domains and thus no uniform dispersion of micro-droplets of water was achieved irrespective of the mechanical stirring process.

3.2.2 Fabrication of pressure sensors

We fabricated two types of pressure sensors based on the porous PDMS films as dielectric layers, one of which was a single cell assembled with two glass substrates and the other was a flexible array with two plastic substrates of poly(ethylene terephthalate) (PET). The electrodes on the inner sides of the glass or PET substrates were made of transparent indium–tin–oxide (ITO). For the single cell, the size of the substrate (or the porous PDMS film as a sensing element on it) was $5 \times 4.45 \text{ cm}^2$, and the area of the ITO electrode as a whole was $8 \times 8 \text{ mm}^2$. For the flexible array, line patterns of the ITO electrodes were prepared on two PET substrates. The two PET substrates were assembled such that the directions of the ITO patterns were perpendicular to each other. Both the width of each ITO pattern and the spacing between two adjacent ITO patterns were 3 mm. For the adhesion of the porous PDMS film to both the bottom and top PET substrates, a thin layer (less than $1 \text{ }\mu\text{m}$) of the PDMS solution was spin–coated on each substrate at the rate of 5000 rpm. After placing the PDMS film between the two PET substrates, the whole sample was cured for 30 min at 100°C to promote the adhesion.

3.2.3 Measurements of porous PDMS films and pressure sensors

The distribution of the micro-pores in each PDMS film ($c_w = 0, 0.05, 0.1, 0.15, 0.2, 0.25, \text{ or } 0.3$) was determined from the cross-sectional image obtained using a field emission-scanning electron microscopy (FE-SEM; S-4800, Hitach. In order to examine the transparency of the PDMS film, the transmission spectra in the visible range were measured using a commercial spectrometer (V530, Jasco). In characterizing the single cell of the sensor, the pressure range was varied from 0.02 to 5 kPa.

For measuring the performance of the array of the sensors, pressure was applied using a weight of glass ($7 \times 7 \text{ mm}^2$, 100 mg). The electrical characteristics and the dynamic responses of the two types of the pressure sensors were measured using an impedance analyzer (HP 4192A, Agilent Technologies) and a semiconductor parameter analyzer (4200-SCS, Keithley Instruments), respectively, at room temperature under ambient environment.

3.3 Results and Discussion

3.3.1 Characteristics of porous PDMS films

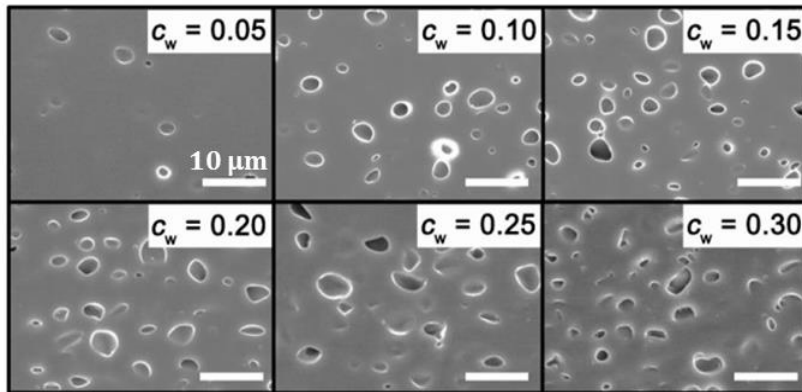


Figure 3.2 The SEM images of six different porous PDMS films prepared from the mixtures of the PDMS and water with the weight ratio of water (c_w) ranging from 0.05 to 0.3. The white scale bars represent 10 μm .

Figure 3.2 shows the cross-sectional FE-SEM images of six different porous PDMS films prepared from the mixtures of the PDMS and water with various values of c_w ranging from 0.05 to 0.3. As shown in the FE-SEM images, the pore density in the PDMS film increased with increasing c_w . As shown in Fig. 3.3, the porosity of the PDMS film calculated from the FE-SEM images was found to be nearly proportional to c_w , indicating that the porosity can be easily varied with c_w .

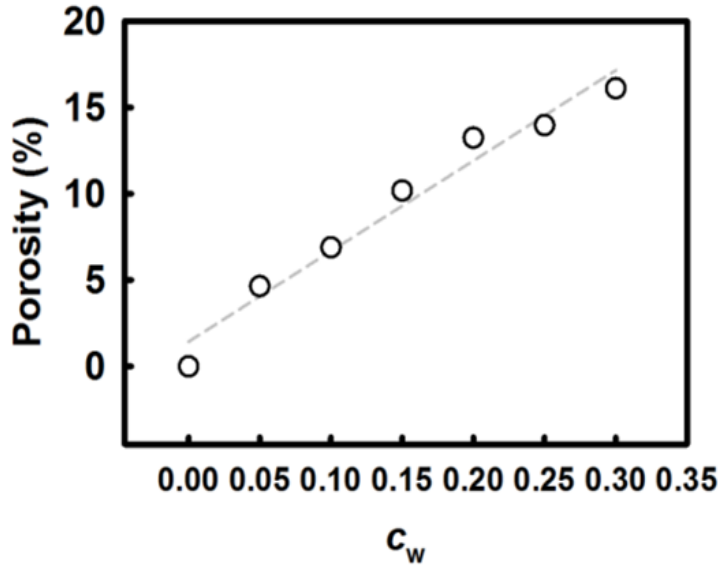


Figure 3.3 Porosity of the fabricated PDMS films as a function of c_w .

Furthermore, the thickness of the PDMS film can be easily controlled by adjusting the height of the spacer as shown in Fig. 3.4. Histogram of the diameter distribution of micro-pores in the PDMS film with $c_w = 0.3$ was obtained from Fig. 3.5(a) using an image processing program. The average pore diameter was measured to be about $2 \mu\text{m}$, and the standard deviation is about $4 \mu\text{m}$. As shown in Fig. 3.5(b), the most dominant pore diameter is sub-micrometer scale. It can be seen that the pores are evenly distributed over the whole area of the film.

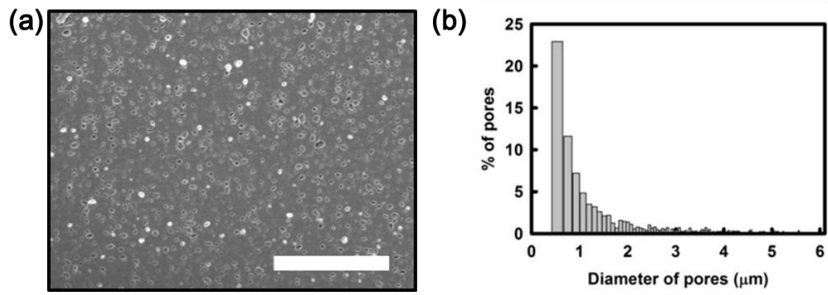


Figure 3.4 (a) The cross-sectional image of a portion of the porous PDMS film with $c_w = 0.3$, observed with the SEM. The scale bar represents 100 μm . (b) Histogram of the diameter distribution of pores obtained from (a).

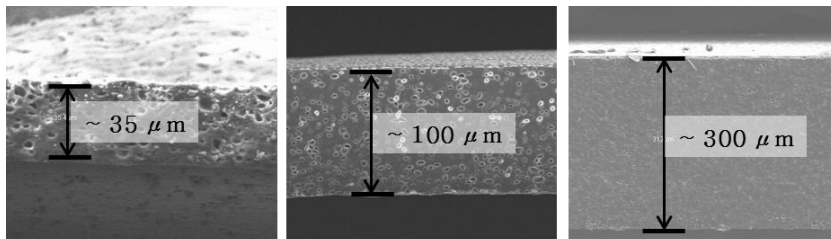


Figure 3.5 The SEM images of the porous PDMS film with various thickness.

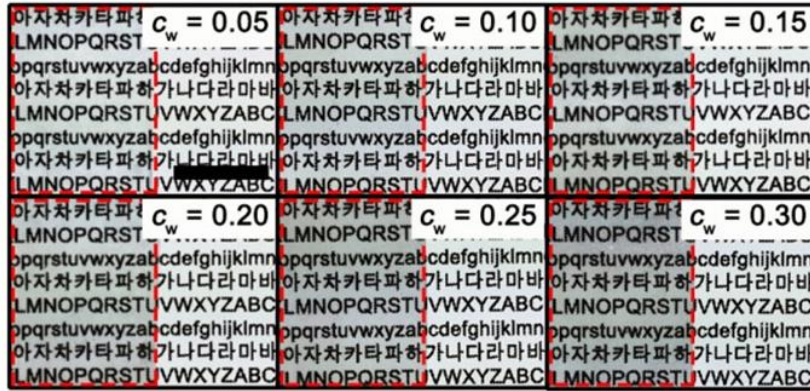


Figure 3.6 Photographic images of the six PDMS films showing the dependence of the transparency on c_w under ambient light. The rectangular region enclosed by red dashed line in each sample represents the region of the porous PDMS film. A transparent sheet with three types of characters (Korean letters and block alphabets together with small alphabets in English) was placed between an illuminating light source and the PDMS film. The black scale bar is 1 cm. The size of the PDMS region is $1.5 \times 2 \text{ cm}^2$.

As for a variety of sensing applications [17, 49], we first examined the optical transmission properties of six different PDMS films prepared from the mixtures of the PDMS and water with c_w from 0.05 to 0.3. For the transmission measurements, a transparent sheet with three types of characters (Korean letters and block alphabets

together with small alphabets in English) was placed between an illuminating light source and the porous PDMS film. In Fig. 3.6, the rectangular region enclosed by red dashed lines in each sample represents the region of the porous PDMS. The transparency of the PDMS film was decreased as c_w was increased. Fig. 3.6 shows the transmission spectra of the six porous PDMS films, compared to the bare film with no micro-pores, in the visible range.

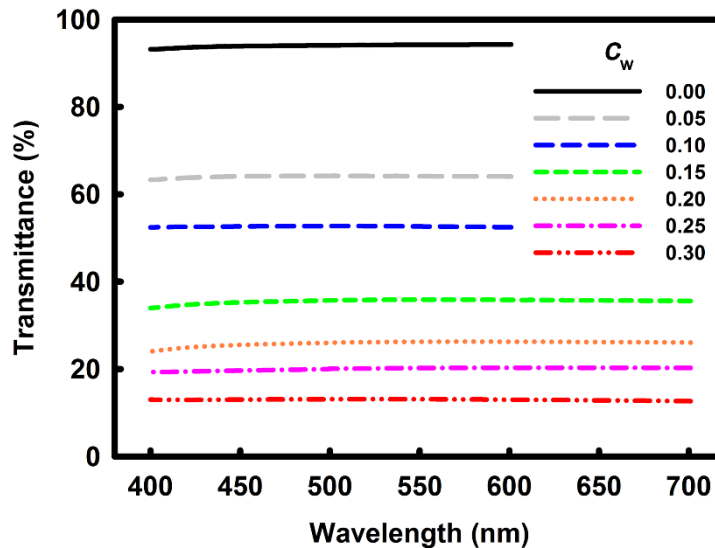


Figure 3.7 The dependence of the transmittance of the PDMS films on c_w from 0 to 0.3 in the visible range.

As shown in Fig. 3.7, the values of the transmittance for $c_w = 0, 0.05, 0.1, 0.15, 0.2, 0.25,$ and 0.3 were measured to be 94, 64, 53, 36, 26, 20, and 13%, respectively, at the wavelength of 550 nm. No

appreciable dependence of the transmission on the wavelength was observed in the whole visible range. In fact, the porosity-dependent transparency is mainly attributed to light scattering caused by micro-pores in the film and can be increased with decreasing the pore size down to be less than the range of the visible light.

3.3.2 Performance of single cell-type of pressure sensor

The performance of the single cell-type pressure sensor based on the porous PDMS films was evaluated. The capacitance values of the pressure sensors fabricated with seven different c_w (0, 0.05, 0.1, 0.15, 0.2, 0.25, and 0.3) were measured as a function of the applied pressure using an impedance analyzer. For the sensing characteristics, the relative capacitance change (ΔC) to the initial capacitance (C_0) under no pressure was plotted as a function of the applied pressure in Fig. 3.8. Note that for each c_w , three different samples were used for the measurements and the error was within 8.5%. As clearly seen from Fig. 3.8, the pressure sensor with micro-pores exhibited a much larger change of the capacitance than that with no pores.

The capacitance change became increased initially and saturated in the high pressure regime.

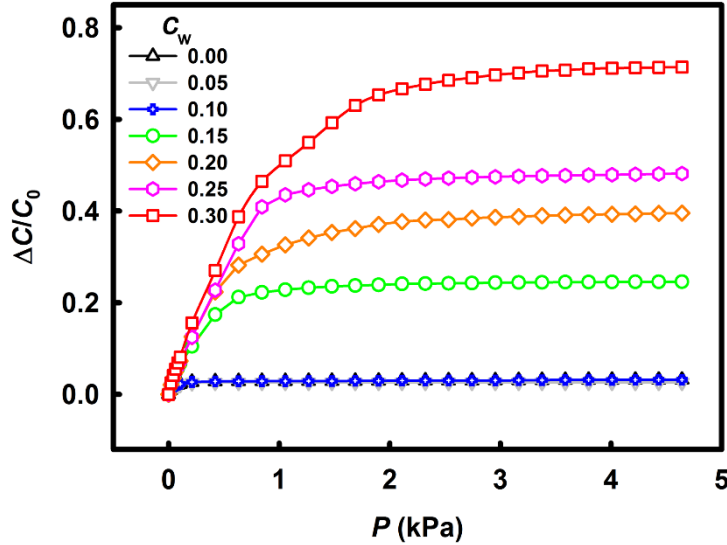


Figure 3.8 The relative capacitance change (ΔC) to the initial capacitance under no pressure (C_0) as a function of the applied pressure. Note that for each c_w , three different samples were used for the measurements. The error was within 8.5 %.

In describing the porosity effect of the dielectric layer of the PDMS on the performance of the sensor, the sensitivity ($S = \delta (\Delta C/C_0) / \delta P$ with the applied pressure P), particularly, in the low pressure range from 0 to 0.1 kPa ($S_{0.1}$) was presented in Fig. 3.9 for various values of c_w . The higher porosity of the dielectric layer was found to yield the higher sensitivity. The sensitivity of the sensor with $c_w > 0.15$ was at least three times larger than that with $c_w < 0.1$. This suggests that the pore density in the PDMS film should be

sufficiently high to produce the deformability and the elasticity of the dielectric layer in the pressure sensor. Apart from the pore density, the average size of the pores will also influence the sensitivity of the pressure sensor from the viewpoints of the deformability and the elasticity.

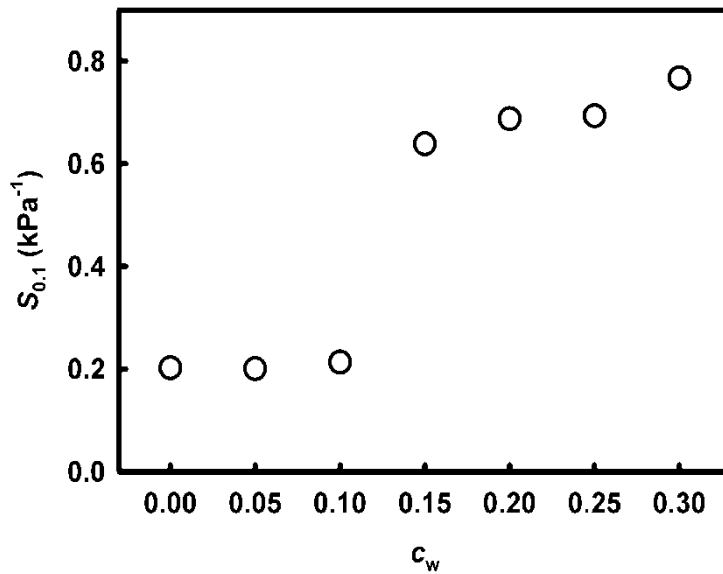


Figure 3.9 The sensitivity ($S_{0.1}$) in the low pressure range from 0 to 0.1 kPa as a function of c_w .

Let us describe more details of the performance of our pressure sensors in terms of the sensitivity and the dynamic response. Figure 3.10 shows the pressure sensitivity S as a function of the applied pressure ranging from 0 to 5 kPa, determined from the slope of the graph at given pressure for each c_w in Fig. 3.8.

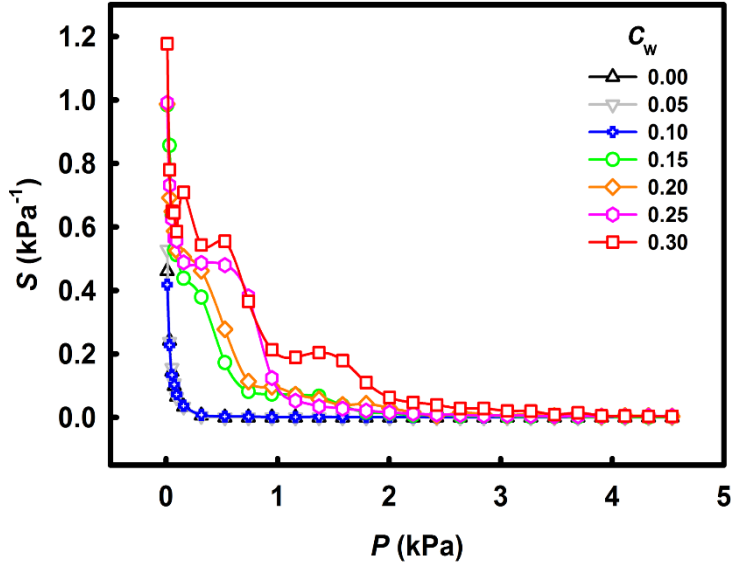


Figure 3.10 The values of the pressure-dependent sensitivity S of our sensors with different PDMS films as a function of the applied pressure.

For the case of $c_w = 0.3$, the sensitivity of about 1.18 kPa^{-1} was obtained in the pressure range below 0.02 kPa , which is much higher than most of existing capacitive-type sensors as summarized in Table 3.1. This value is comparable to the sensitivity of an advanced sensor with nano-needle structures [51]. As shown in Fig. 3.10, in contrast to the non-porous sensor ($c_w = 0$) which is sensitive only in the very low pressure range ($< 0.5 \text{ kPa}$), the porous case exhibited the moderate sensitivity in the intermediate pressure range up to about 2 kPa , meaning that the observed pressure-dependent sensitivity would be useful for more sophisticated applications such as e-skin. Note that our pressure sensor has a relatively narrow

measurement range compared to those based on an air gap [17, 18, 47], uniform elastic materials [14–16, 48–50], or complex nano- or micro-structures [19, 51] as shown in Table 3.1, but it is simpler to construct in array and easier to implement into flexible systems. And the narrow range could be improved by increasing the porosity of elastomer film or using other materials with higher elasticity.

Table 3.1 The main characteristics of various capacitive-type pressure sensors.

Types	Electrode	Dielectric layer	d^{**} (μm)	Maximum sensitivity (kPa^{-1})	Linear range (kPa)	Measurement range (kPa)
Air gap	ITO [17]	Air/SU-8	13	0.037	0–100	0–800
	Au–Cu [47]	Air	15	0.0023	0–56	0–720
	Cu [14]	Air/PDMS	12	0.0048	0–200	0–600
Elastic material	Ag NW [16]	Ecoflex	500	0.0016	0–500	0–1400
	Cu [14]	PDMS	90	0.22×10^{-4}	240–1000	240–1000
	Cu [48]	PDMS	30	0.0019	0–945	0–945
	Pt–Au [15]	PDMS/parylene	11	0.024	0–10	0–140
	AgNW [49]	PDMS	~ 500	4.0×10^{-4}	0–50	0–260
	CNT [50]	Ecoflex	~ 500	5.9×10^{-4}	10–150	10–150
Micro-/ nano-structure	ITO [19]	Pyramid structure	6	0.55	0–1.5	0–7
	Al [51]	Nano-needle structure	1.6	1.76	0–0.2	0–7
Our work	ITO	Porous PDMS	100	1.18	0–0.02	0–5

** The thickness of dielectric layer

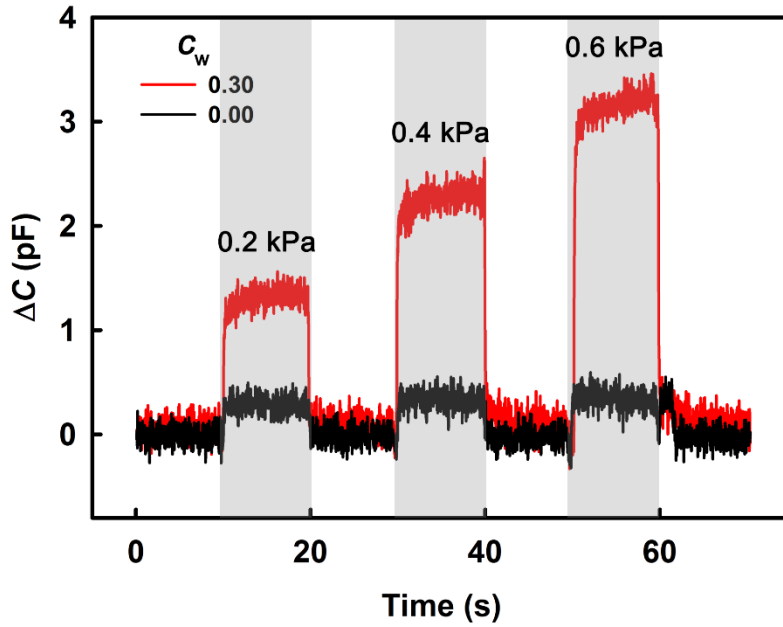


Figure 3.11 The dynamic responses of two pressure sensors, fabricated using the porous PDMS films with $c_w = 0.0$ (black) and 0.3 (red), under the pressure of 0.2, 0.4, and 0.6 kPa for 10 s each.

We discuss the dynamic responses of two pressure sensors with the PDMS ($c_w = 0$ and 0.3) to three different values of the applied pressure in sequence (0.2, 0.4, and 0.6 kPa for 10 s each). The initial values of C_0 for $c_w = 0$ and 0.3 were measured to be 15 and 10 pF. As shown in Fig. 3.11, for the sensor with $c_w = 0.3$, the values of ΔC were 1.24, 2.14, and 3.01 pF under the pressure of 0.2, 0.4, and 0.6 kPa, respectively. For the case of $c_w = 0$, however, ΔC was not substantially changed (0.30, 0.33, and 0.36 pF) as expected.

Although there is drifting of ΔC for 10 s under the pressure for $c_w = 0.3$, this variation is practically negligible compared to the increase by applying the pressure, so that the slight increase of ΔC during pressing rarely affects the accuracy of pressure sensing.

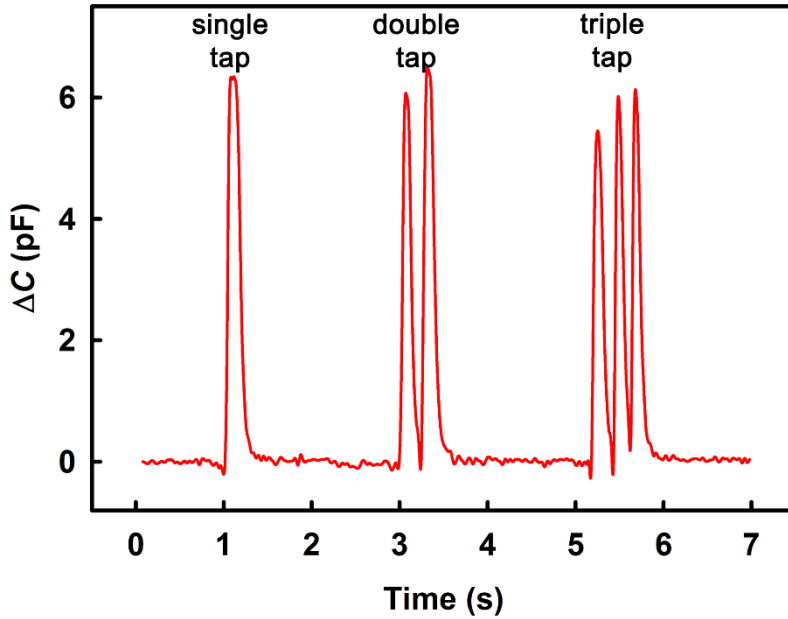


Figure 3.12 The temporal response of the pressure sensor for $c_w = 0.3$ to consecutive taps.

The average response time over the rising and falling times was less than 150 ms. Fig. 3.12 shows another characteristic response of our pressure sensor with the porous PDMS ($c_w = 0.3$) to consecutive taps. Our sensor was found to respond well to a single tap in 250 ms, double taps in 400 ms, and triple taps in 700 ms, which clearly demonstrated the temporal accuracy of the sensor that means consecutive taps in the short times can be resolved by the sensor.

3.2.3 Performance of flexible array of pressure sensors

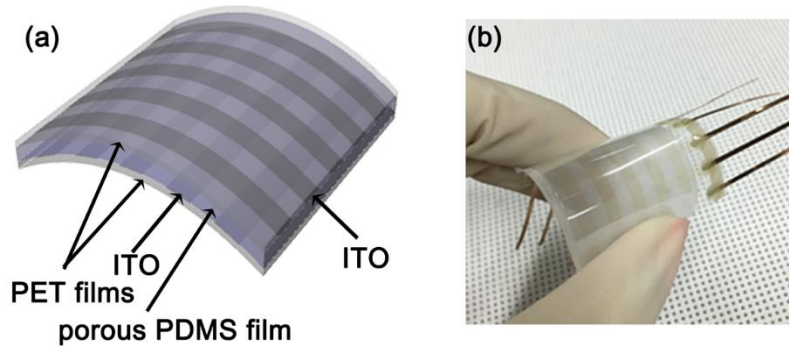


Figure 3.13. (a) A schematic diagram and (b) a photographic image of our 5×5 array ($3.3 \times 3.3 \text{ cm}^2$ in size) of flexible pressure sensors based on the porous PDMS film with $c_w = 0.3$ between two ITO-coated flexible PET substrates.

For applications in touch panels and electronic skins, we fabricated a prototype array of 5×5 flexible pressure sensors based on the porous PDMS layer with $c_w = 0.3$ using two ITO-coated flexible PET substrates as shown in Fig. 3.13(a). The patterned ITO electrodes on the inner surfaces of the two substrates were placed perpendicular to each other. Each elemental sensor was defined by the region covered with the opposing electrodes. Fig. 3.13(b) shows the actual deformation of the flexible sensor array ($3.3 \times 3.3 \text{ cm}^2$ in size) we fabricated.

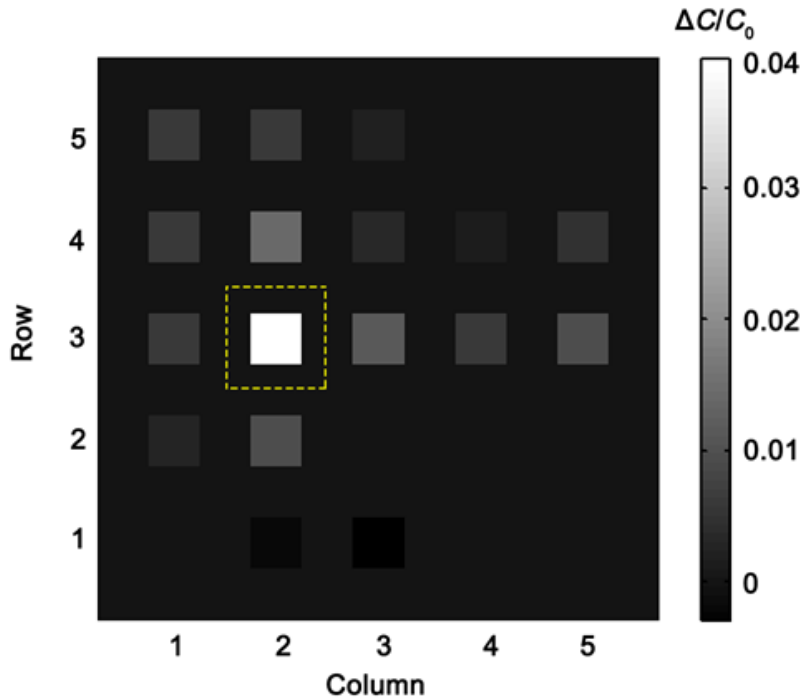


Figure 3.14 The distribution of the capacitance change in the sensor array upon placing a weight of glass ($7 \times 7 \text{ mm}^2$, 0.02 kPa) in the rectangular region enclosed by the yellow dotted line. The gray level in the bar scale represents the magnitude of the relative capacitance change.

The capacitance change ($\Delta C/C_0$) over the whole area of the sensor array under the pressure of 0.02 kPa , exerted by a weight of glass placed in row 3 and column 2 (the region enclosed by the yellow dotted line), was measured and shown in the gray level representation in Fig. 3.14. A level of the brightness corresponds to the magnitude of the capacitance change in the gray level

representation. Although the propagation of pressure from a selected element to non-selected, adjacent elements (or the crosstalk between neighboring elements) was observed to some extent in our prototype, it can be easily eliminated through the isolation of the elements by either patterning the PDMS layer or using a different type of the flexible substrate such as rubber or fabric, not plastic.

3.4 Summary

A capacitive-type flexible pressure sensor with the high sensitivity and the multi-level capability in the intermediate pressure regime was developed using an elastomer film with micro-pores as a dielectric layer. The uniform dispersion of micro-pores in the elastomer matrix was achieved through the phase-separation between a prepolymer material of the PDMS and an insoluble solvent of water in solution. The porous PDMS was found to allow the low elastic modulus and high deformability. As a consequence, the pressure sensor with the porous PDMS showed the sufficiently high and pressure-dependent sensitivity in a relatively low range of pressure (< 5 kPa). In our phase-separation approach, the sensitivity of the pressure sensor can be easily tailored in terms of the porosity of the PDMS by altering the weight ratio of water in a mixture of PDMS and water. As demonstrated in the prototype of our flexible pressure sensor array, the porous PDMS film will be applicable for advanced touch panels with more human-friendly interfaces and skin sensors detecting small changes in pressure.

Chapter 4

Highly Efficient, Flexible, and Transparent Triboelectric Nanogenerator

4.1 Introduction

With the rapid development of internet of things and wireless sensor networks, an energy-harvesting device from ambient environment has recently gained considerable attention for its potential role in the independent and sustainable operation of electronic devices [54–57]. Especially, such energy harvesting devices with high flexibility/stretchability as well as transparency have a great potential to realize fascinating applications ranging from transparent electronic skins to self-powered wearable electronics as shown in Fig. 4.1 [58–63].

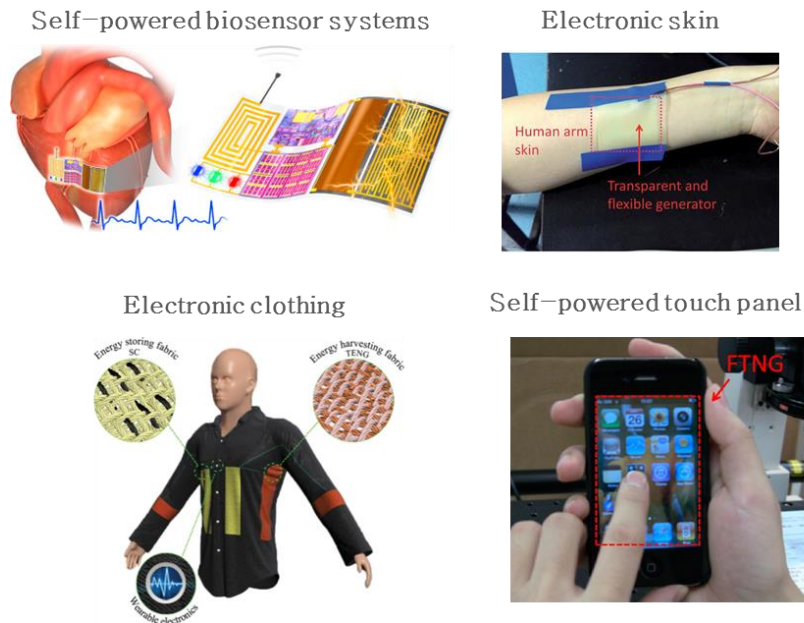


Figure 4.1 Various applications for flexible and transparent energy harvesting devices.

Among a variety of energy-harvesting technologies, TENG based on a contact electrification and an electrostatic induction has been extensively investigated due to the numerous advantages such as the cost-effectiveness, the fabrication simplicity, the robustness, the small volume, and the high efficiency [20, 64, 65]. In general, the output performance of TENG is mainly determined by the amount of transferred tribocharges between two contact surfaces during contact [65, 66]. Considerable efforts have been made to enhance the output performance of TENG by selecting combinations of contact materials having a large difference in the triboelectric polarity [67–

76], introducing micro-/nano-structures on the contact surface [67–69, 76–82], and utilizing a conducting layer both as a contact material and an electrode [67, 68, 70].

In the previous studies of a flexible and transparent TENG (FT–TENG), ITO [82–84] and graphene [72, 85] were chosen as both contact materials and electrodes instead of opaque and brittle metals. They tried to improve the output performance through surface engineering, but the level of output power is still too low to be commercially implemented. It remains a challenge to achieve the high output performance while preserving both the transparency and the flexibility.

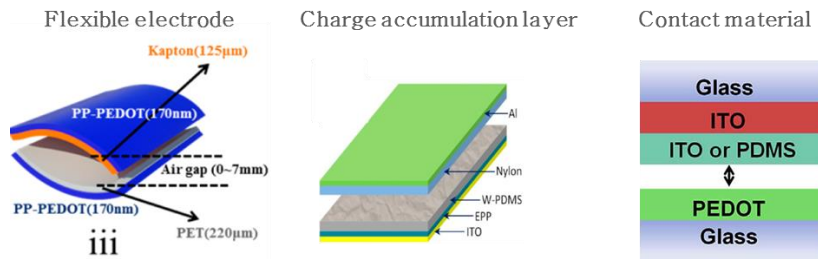


Figure 4.2 Previous work of PEDOT:PSS–based TENGs (Ref. [86–66]).

In this work, we demonstrated a novel concept of highly efficient FT–TENG which is based on a conducting polymer layer embedding nano-wires. It is reported for the first time that PEDOT:PSS is suitable for an electron–accepting contact material (tribo–negative material) owing to its high electronegativity. Note that PEDOT:PSS in TENGs had been only served as a charge accumulation layer [86]

and a flexible electrode [87], and recently started to use as a contact material [88, 89] as shown in Fig. 4.2.

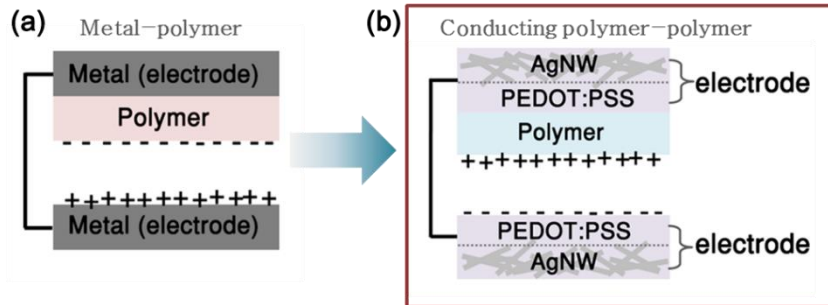


Figure 4.3 Schematics showing (a) a metal–polymer combination of the conventional TENG, (b) a proposed design composed of a conducting polymer and silver nanowires for FT–TENG.

Here, we systematically studied the triboelectric characteristic of PEDOT:PSS by scanning Kelvin probe microscopy (SKPM) where PEDOT:PSS was found to show an excellent electron–accepting characteristic. Contrary to the metal–polymer combination (Fig. 4.3(a)), the superb electron–accepting characteristic of PEDOT:PSS allows diverse electron–donating materials as an opposite contact layer so that the output level can overcome previous limitations. Furthermore, the increase of the surface area resulting from the silver nanowire (AgNW) layer placed beneath a PEDOT:PSS layer was found to further enhance the output performance. To the best of our knowledge, our FT–TENG (Fig. 4.3(b)) shows the highest output power compared to previous FT–TENGs. Our FT–TENG built

on a stretchable substrate exhibits a high transparency and the excellent output performance even on a random surface like a skin or a fabric.

4.2 Experimental Details

4.2.1 Materials and sample preparation

A PEDOT:PSS aqueous solution (Celvios™ PH1000, Heraeus) was mixed with 5% of ethylene glycol and 1% of fluorosurfactant (Zonyl FSO, Sigma–Aldrich) for the conductivity [90] and wettability [91] enhancement, respectively. For the uniform formation, the substrates (glass, PEN, PDMS) were treated with ultraviolet ozone (UVO) for 20 min before the coating process. Note that the UVO treatment helps to increase the wettability of the surface and the adhesion between the film and substrate. A prepared PEDOT:PSS solution was spin–coated on UVO–treated substrates at a speed of 2000 rpm. And then, the substrate was annealed at 130 °C for 15 min to evaporate any remaining solvents. A 0.3% of AgNW aqueous solution (DT–AGNW–N30–DI, Ditto Technology Co., Ltd.) was spin–coated on an UVO–treated glass substrate at the rate of 1000 rpm, and it was then annealed at 130 ° C for 15 min. In the case of the PEDOT:PSS/AgNW film, AgNW and PEDOT:PSS were coated on an UVO–treated substrate as mentioned above, sequentially. A poly(urethane acrylate) (PUA; MINS–301RM, Minuta tech.) film utilized as an opposite contact material of PEDOT:PSS was prepared by spin–coating with a speed of 500 rpm and UV curing for 1 min. In the final structure of FT–TENG, the microstructure was formed on the surface through a cloth used as mold. For the comparison of

triboelectric properties of contact electrodes, each 30 nm thick Al, Ag and Au films on a glass substrate were also prepared by thermal evaporation under about 10^{-6} Torr. Here, an ITO-coated on a glass or on a PEN is commercially available. For the preparation of the 200 μm thick of a PDMS film used for a stretchable substrate, a PDMS prepolymer (Sylgard 184, Dow Corning), mixed with a curing agent at the weight ratio of 10:1, was placed between two glass substrates that were treated to be hydrophobic by spin-coating a solution of a chemically inert fluoropolymer (DS-1120F, HARVES Co., Ltd.). The gap between the two substrates was maintained using two layers of 100 μm thick tape spacers. The assembled sample was heated at the curing temperature of the PDMS prepolymer (70°C) for 3 h to achieve the thermal cross-linking of the PDMS. The PDMS film was finally detached from the substrates without any mechanical damage owing to the strong hydrophobic nature of the fluoropolymer used. This process for free-standing PDMS film was referred to previously developed method [92].

4.2.2 Measurement and characterization

The SKPM measurements were performed using an atomic force microscope (AFM; XE-100, Park Systems) with a Pt-coated tip with the scan size of 5 μm . The experimental setup of the SKPM is as shown in Fig. 4.4.

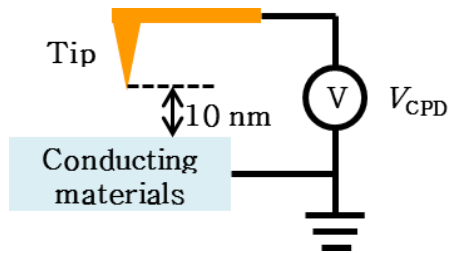


Figure 4.4 Experimental setup of the SKPM measurement by AFM.

The oscillation amplitude, phase and resonance frequency for the SKPM measurement were 2 V, 90° and 17 kHz, respectively. The tip-to-sample distance was 10 nm in the SKPM mode. The surface morphology was also measured by AFM with the scan size of 4 μ m. The sheet resistances of ITO, PEDOT:PSS, PEDOT:PSS/AgNW were measured by the four-point probe method. In order to compare the transparency of ITO on PEN and PEDOT:PSS/AgNW film on PDMS, the transmission spectra in the visible range were measured using a commercial spectrometer (Ocean Optics). A digital oscilloscope (Waverunner 6030, Lecroy) and a low-noise current preamplifier (SR570, Stanford Research Systems) were used to measure the output signals generated from the TENGs. The output performance of the FT-TENGs without/with the AgNW layer was measured using a digital oscilloscope under the applied pressure of 3.5 N with the frequency of 5 Hz. All measurements were performed under ambient environment.

4.3 Triboelectric Property of PEDOT:PSS

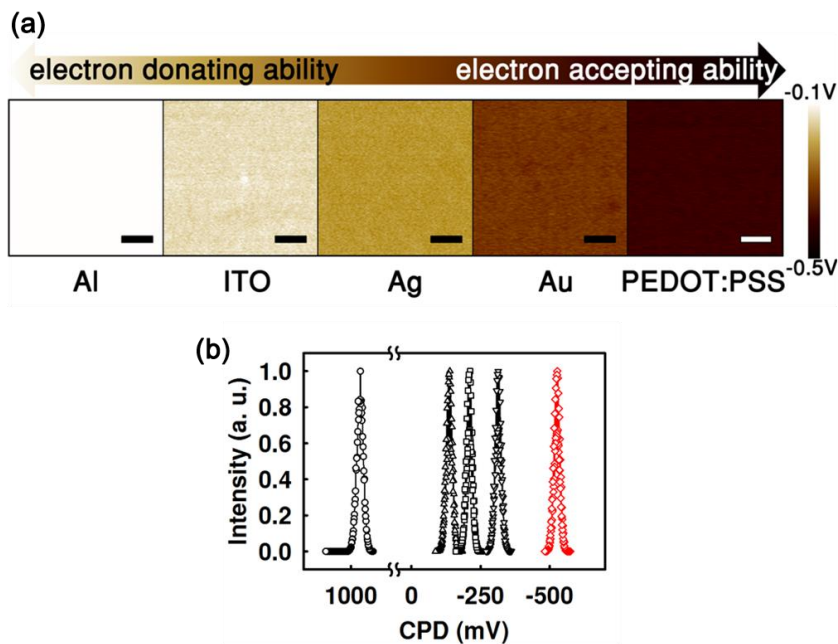


Figure 4.5 (a) SKPM images and (b) histogram distributions of contact potential difference (CPD) for the tribo-materials obtained from AFM measurements. The scale bars indicate 1 μ m.

The surface potential of PEDOT:PSS was measured with a comparison of commonly used conducting materials (Al, Ag, Au, and ITO) using SKPM for identifying the triboelectric characteristics. Figure 4.5(a) shows the distribution image of a surface contact potential difference (CPD) between a contact surface and a Pt tip for the five-triboelectric materials. The average CPDs of Al, ITO, Ag, Au, and PEDOT:PSS were measured to be about +955, -136, -208, Au, and PEDOT:PSS were measured to be about +955, -136, -208,

-313, and -526 mV, respectively as shown in Fig. 4.5(b). It is well known that the tendency to donate or attract electrons can be seen through the CPD [93, 94]. The larger value of CPD means that it has a stronger tendency to donate electrons, and vice versa. Al is predicted to have the strong tendency to donate electrons, and it has been usually used as an electron-donating contact material of TENG [67]. However, it is not suitable for the FT-TENG because of its brittleness and opaqueness. On the other hand, PEDOT:PSS, which is expected to have a tendency to attract electrons from the CPD data, is an appropriate material for the FT-TENG owing to its advantages of the transparency and the flexibility.

To verify the correlation between the tendency obtained from SKPM data and the output performance of TENG, the basic devices were fabricated as shown in Fig. 4.6(a).

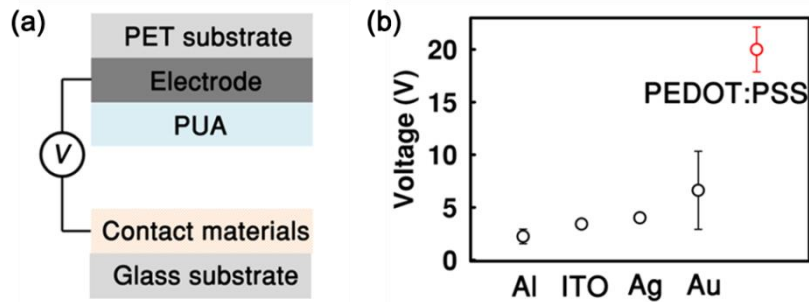


Figure 4.6 (a) The schematic illustration and (b) the output voltage of the basic TENGs based on five-triboelectric materials.

Here, PUA elastomer was used as an opposite contact layer because of its strongly electron-donating characteristic as well as

the high transparency, the flexibility, and the ease of fabrication. All conducting contact materials (triboelectric materials) were deposited on a glass substrate, and PUA film was formed on a plastic substrate, PEN. We measured the output voltage using a digital oscilloscope under a compressive force of 0.7 kgf. Fig. 4.6(b) shows the output voltage of TENGs based on five-triboelectric materials. The output voltages of each device based on Al, ITO, Ag, Au and PEDOT:PSS were measured to be 2.3, 3.4, 4.0, 6.6 and 20.0 V, respectively. The TENG based on Al shows the lowest output-voltage while that based on PEDOT:PSS shows the highest output-voltage. It agrees well with the SKPM data since PEDOT:PSS has the largest difference of CPD with the strong electron-donating PUA.

4.4 Effect of AgNWs on Output of TENG

In our FT-TENG, an AgNW layer was coated beneath the PEDOT:PSS layer for the enhancement of both the electrical property and the effective contact area of the contact layer. Nanowires can serve as good fillers for conducting polymer. It has been reported that incorporating of nanowires into conventional conducting polymers improves the conductivity of nanowires/polymer composites by many orders of magnitude [95], which could be attributed to nanowires' large contact area, high dimensional aspect ratio, and exceptional electrical conductivity [96].

4.4.1 Surface roughness

First, the surface roughness of the PEDOT:PSS, the AgNW, and the PEDOT:PSS/AgNW films was analyzed using atomic force microscopy (AFM) as shown in Fig. 4.7(a). The root mean square roughness (R_q) of the PEDOT:PSS film was observed to be 2.99 nm, whereas that of AgNW film was observed to be 15.17 nm owing to the large diameter of 30 nm of AgNWs. The R_q of the hybrid film was 9.54 nm, which is lower than that of the AgNW film, but it is about 3 times higher than the PEDOT:PSS film. Figure 4.7(b) shows the roughness profiles of three films. Contrary to the smooth surface of PEDOT:PSS film, the surface profile of PEDOT:PSS/AgNW hybrid

film follows that of nanowire mesh beneath of the PEDOT:PSS. Note that the increase of the surface roughness in nanoscale as well as microscale can enlarge the effective contact area and enhance the power output performance of TENGs [97]. Therefore, the increased surface roughness resulting from an additional layer of AgNW is expected to contribute to the enhancement of TENG performance.

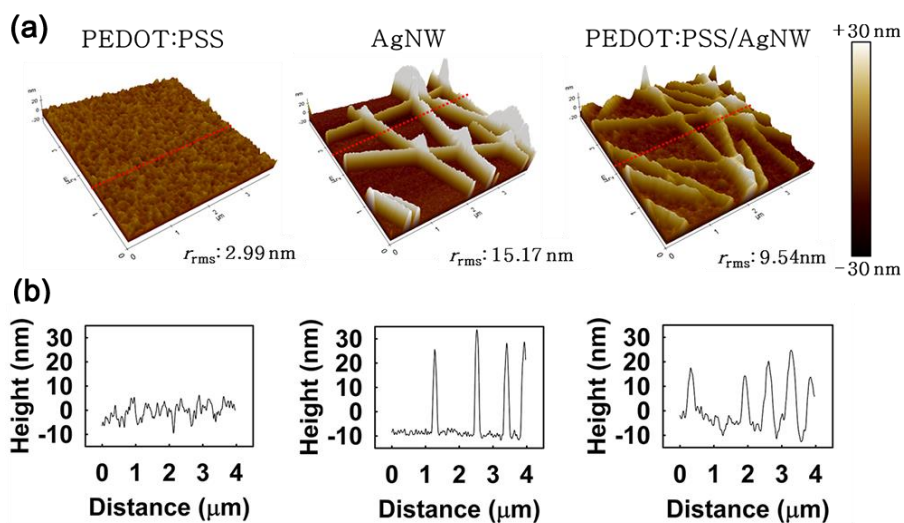


Figure 4.7 (a) AFM 3D topographic images of PEDOT:PSS, AgNW and PEDOT:PSS/AgNW surfaces. (b) Line scan profiles corresponding to the red dashed lines in (a).

4.4.2 Sheet resistance

Second, the electrical characteristic of the PEDOT:PSS and the PEDOT:PSS/AgNW hybrid films was observed as shown in Fig. 4.8. The sheet resistances (R_{sq}) of the ITO, the PEDOT:PSS, the PEDOT:PSS/AgNW films were measured to be about 54.5, 189.2, 157.2 Ω /sq, respectively. Compared with the PEDOT:PSS film, The R_{sq} of the hybrid film was reduced by about 22 % through the introduction of the AgNW layer placed beneath the PEDOT:PSS layer. It is reported that the decrease in the sheet resistance of the contact electrode contributes to the improvement in the output performance of TENG [89]. Although this improved value is still higher than that of ITO, which is usually used as an transparent electrode, the sheet resistance can be further reduced through the increase of the AgNWs density and the multi-coating of PEDOT:PSS layers.

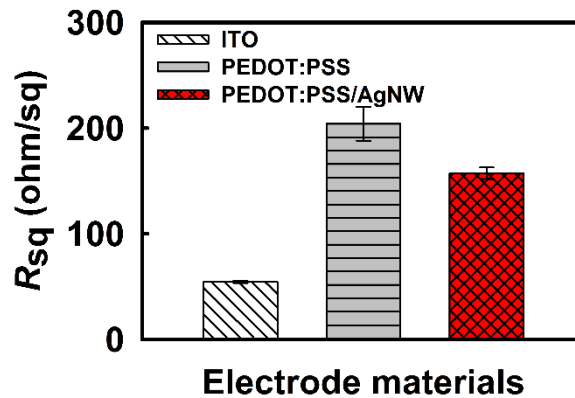


Figure 4.8 Sheet resistance for ITO, PEDOT:PSS and PEDOT:PSS/AgNW films.

4.5 Characteristics of PEDOT:PSS/AgNW Film

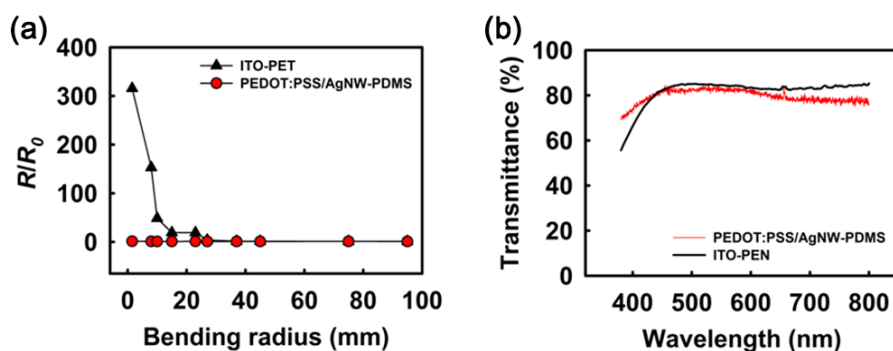


Figure 4.9 (a) Normalized resistance over the bending radius and (b) transmission over the wavelengths 380–780 nm for ITO on PEN (black) and PEDOT:PSS/AgNW on PDMS (red).

The mechanical and optical properties for the PEDOT:PSS/AgNW hybrid film as a flexible and transparent electrode were analyzed. A mechanical bending test for PEDOT:PSS/AgNW film coated on PDMS was performed with comparison of ITO on PEN as detailed in Fig. 4.9(a). The resistance of ITO increased drastically at less than 30 mm of a bending radius. Compared to ITO, the resistance of the PEDOT:PSS/AgNW film remained unaltered even with a bending radius of 1.5mm. The PEDOT:PSS/AgNW film was found to be quite stable under bending

radius unlike ITO film owing to the mechanical flexibility of a polymer. Figure 4.9(b) shows the transmission spectra of the ITO on PEN and the PEDOT:PSS/AgNW film on PDMS in the visible range. The values of the transmission were 84.5 and 82.5 %, respectively, at the wavelength of 550nm. It is shown that the transparency of PEDOT:PSS/AgNW/PDMS film is as high as ITO/PEN film. Figure 4.10 shows the photographic image of PEDOT:PSS/AgNW film on PDMS on the back of a hand. Our elastomeric film makes conformal contact with a curved surface like skin compared to rigid or plastic substrates.

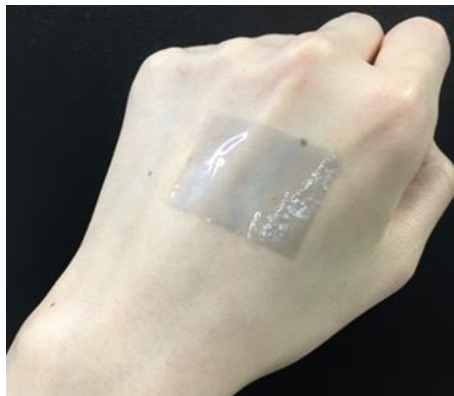


Figure 4.10 Photographic image of PEDOT:PSS/AgNW/PDMS film on a curved skin surface.

4.6 Output Performance of FT-TENGs

We examined the output performance of the FT-TENG composed of the PEDOT:PSS film or PEDOT:PSS/AgNW hybrid film as the contact layer and an electrode, and a PUA film as the opposite contact layer. The microstructure was also introduced on the PUA surface for the enlargement of the friction area by using a fabric having natural roughness through an imprinting method of soft lithography without any additional photolithography process. As mentioned earlier, this simple approach further improves the output performance by increasing the effective contact area [79].

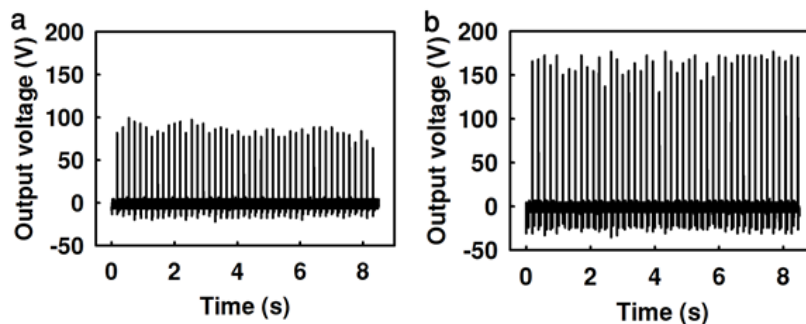


Figure 4.11 The output voltage of the TENG based on (a) PEDOT:PSS and (b) PEDOT:PSS/AgNW layers.

The maximum output voltage of the fabricated TENG based on the PEDOT:PSS film was measured to be approximately 80 V as shown in Fig. 4.11(a). It is a relatively high level of performance compared to the conventional FT-TENG, and it results from the large difference of tribo-electricity between PEDOT:PSS and PUA. Figure 4.11(b) shows the output voltage of our final design of the FT-TENG (Figure 4.3(b)) based on the PEDOT:PSS/AgNW hybrid film. The output voltage was measured to be about 170 V, and it was more than two times higher than that of the TENG without AgNW. The difference between the amount of increased contact area and that of the increased output voltage is mainly due to the un-contacted region under the applied pressure.

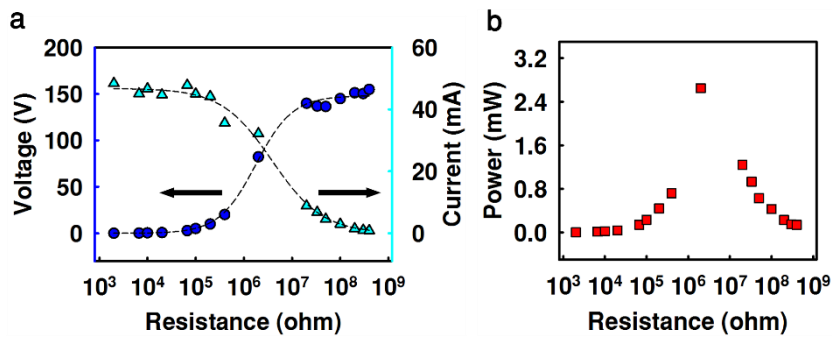


Figure 4.12 (a) The output voltage, the current and (b) the instantaneous power output of the optimized TENG depending on the external load resistance.

To study the effective electric power of the proposed FT–TENG, the open–circuit voltage and the short–circuit current were systematically measured with various external load resistances from 2 k Ω to 400 M Ω as shown in Fig. 4.12(a). It is apparent that the voltage increased with increasing load resistance, whereas the current density dropped due to Ohmic loss. As a result, the maximum instantaneous power density of about 1.5 mW/cm² (\sim 2.6 mW) was achieved at an external resistance of about 2 M Ω (Fig. 4.12(b)), and it is the highest value at more than 15 times the conventional FT–TENGs as known from Table 4.1.

Table 4.1 Summary of TF–TENGs

		Our work	[85]	[83]	[84]
triboelectric materials	+	PUA	Graphene	ITO(Au)	ITO
	–	PEDOT:PSS	nest–like PDMS	PDMS	nano–patterned PDMS
electrode		PEDOT:PSS/AgNW	graphene	ITO	ITO
output voltage (V)		160	271	200	3.8
output current (μ A)		> 50	7.8	7	0.8
maximum instantaneous power density (mW/cm ²)		> 1.5	0.99 x 10 ^{–1}	0.90 x 10 ^{–1}	0.75 x 10 ^{–4}

4.7 Practical Application of FT–TENGs

Next generation of wearable electronics demands the systems directly worn on soft and curved human body that is covered with highly extensible skins (with an average elongation from 3% to 55%). To demonstrate the practical application of our FT–TENG, it was operated at the various circumstances. As seen from Fig. 4.13(a), the PEDOT:PSS/AgNW film on a PDMS substrate was placed on a wrist skin (orange dashed rectangular), and the PUA on a PDMS was attached to a finger (yellow dashed circle). The hybrid film is highly transparent and capable of conformal contact with a random surface like a wrist. The triboelectric voltage generated from a light touch with the finger to the wrist was about 40 V (Fig. 4.13(b)). Also, the PEDOT:PSS/AgNW film on a floor (orange dashed rectangular) and the PUA film on a surface of socks (yellow dashed circle) were contacted each other when walking as shown in Fig. 4.14(a). The output voltage generated by vibrations was measured to be about 3 V, while the value from light and heavy steps were 20 and 40 V, respectively as shown in Fig. 4.13(b). Our device was robust under several repetitive steps without any performance degradation. It can be seen that our FT–TENG works quite stable even on a fabric surface as well as human skin.

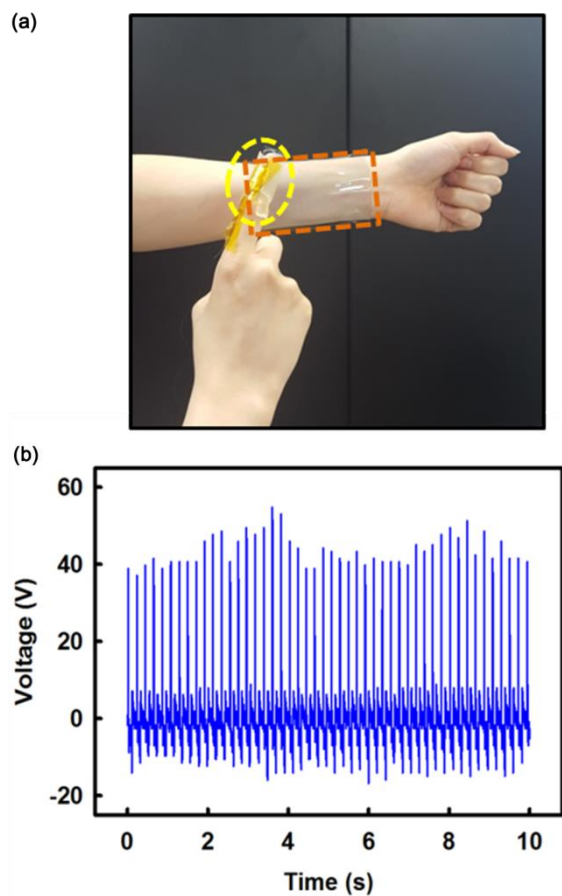


Figure 4.13 Applications of the optimized TENG generated from gentle touch. (a) Photographic images and (b) output voltage of the FT-TENG. The rectangular region enclosed by orange dashed line and the circular region enclosed by yellow dashed line represent PEDOT:PSS/AgNW/PDMS film and PUA/PEDOT:PSS/AgNW/PDMS film, respectively.

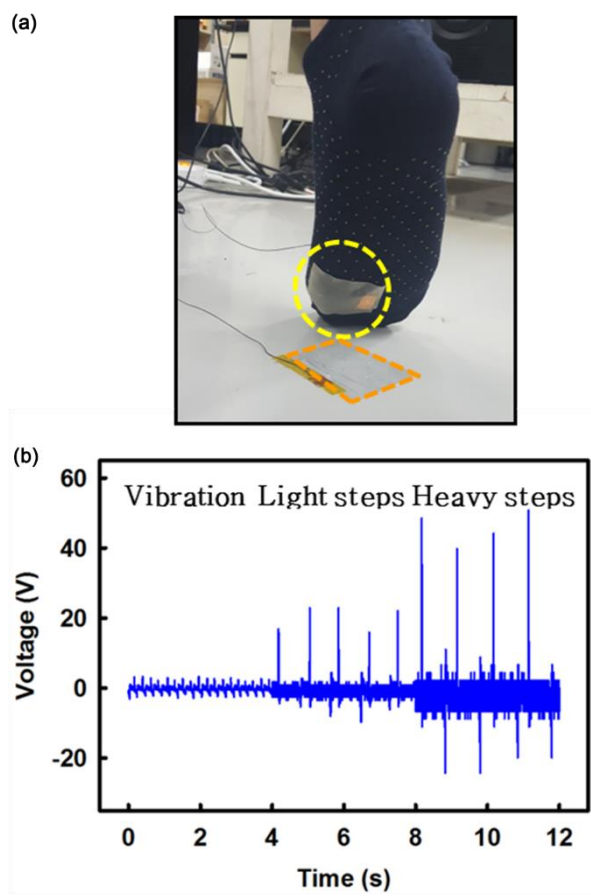


Figure 4.14 Applications of the optimized TENG generated from various steps. (a) Photographic images and (b) output voltage of the FT-TENG. The rectangular region enclosed by orange dashed line and the circular region enclosed by yellow dashed line represent PEDOT:PSS/AgNW/PDMS film and PUA/PEDOT:PSS/AgNW/PDMS film, respectively.

It is also found that the output voltage of our FT-TENG can be changed as a function of the pressure intensity. It has been reported that the effective contact area and can be varied depending on the applied force, and the change of the effective contact area will affect the output performance of TENG [98]. Thus, our FT-TENG can be used as a self-powered pressure sensor.

4.8 Summary

A highly efficient FT-TENG using a PEDOT:PSS/AgNW hybrid film was demonstrated. The high electronegativity of PEDOT:PSS enabled to greatly improve the output performance with an opposite material PUA having a strongly electron-donating characteristic while maintaining both the transparency and the flexibility. Furthermore, the enlargement of the friction area resulting from AgNWs placed beneath a PEDOT:PSS layer contributed to further improve the output power. The final device built on a PDMS substrate exhibited the excellent output performance even on a random surface like a skin or a fabric with the high transparency. This approach will provide a viable and effective framework for developing flexible and transparent power sources in diverse wearable electronics.

Chapter 5

Concluding Remark

In this thesis, the studies on pressure sensors and TENGs suitable for wearable electronics were discussed. Through the understanding and adjusting the physical and geometrical characteristics of major elements determining the device performance, the performance of flexible pressure sensors and TENGs were remarkably improved. In the thesis, the physical properties such as the electrical conductivity and elastic modulus, and the geometrical properties such as roughness and surface area were modified through the utilization of functional polymers and polymer–nanocomposite.

In case of flexible pressure sensors, an elastomer film embedding uniform micro–pores was developed as the dielectric layer of sensors determining the sensitivity. The uniform dispersion of micro–pores in the elastomer matrix was achieved through the phase–separation between a prepolymer material of the PDMS and an insoluble solvent of water in solution. In the phase–separation approach, the sensitivity of the pressure sensor can be easily tailored in terms of the porosity of the PDMS by altering the weight ratio of

water in a mixture of PDMS and water. The porous PDMS was found to allow the low elastic modulus and high deformability. As a consequence, the sufficiently high sensitivity of 1.18 kPa^{-1} in the low pressure range with fast response time of below 150 ms was achieved.

Next, a FT-TENG with high output power was developed through the use of PEDOT:PSS/AgNW hybrid film as the contact electrode determining the output performance. The high electronegativity of PEDOT:PSS enabled to greatly improve the output performance with an opposite material PUA having a strongly electron-donating characteristic while maintaining both the transparency and the flexibility. Furthermore, the increase of the conductivity and friction area resulting from AgNWs placed beneath a PEDOT:PSS layer contributed to further improve the output power. The final device built on a PDMS substrate exhibited the excellent output performance even on a random surface like a skin or a fabric with the high transparency.

The approaches presented through this thesis are promising to play a primary role for the development of advanced wearable electronics with more human-friendly interfaces.

Appendix (acronyms)

IoT: Internet of things

PNG: piezoelectric nanogenerator

TENG: triboelectric nanogenerator

PEDOT:PSS: poly(3,4-ethylenedioxythiophene): poly(sulfonic acid)

CP: conducting polymers

PEDOT: poly(3,4-ethylenedioxythiophene)

PSS: poly(sulfonic acid)

ITO: indium-tin-oxide

AgNW: silver nanowire

UV: ultra violet

PDMS: polydimethylsiloxane

e-skin: electronic skin

DI: deionized

FE-SEM: field emission-scanning electron microscopy

FT-TENG: flexible and transparent TENG

AFM: atomic force microscopy

SKPM: surface Kelvin probe microscopy

UVO: UV ozone

PUA: polyurethane acrylate

Bibliography

- [1] Y. Wan *et al.*, "Recent progresses on flexible tactile sensors," *Mater. Today Phys.*, **1**, 61–73, (2017).
- [2] M. Ha *et al.*, "Triboelectric generators and sensors for self-powered wearable electronics," *ACS nano*, **9**, 3421–3427, (2015).
- [3] Y. Zang *et al.*, "Advances of flexible pressure sensors toward artificial intelligence and health care applications," *Mater. Horizons*, **2**, 140–156, (2015).
- [4] C. Metzger *et al.*, "Flexible-foam-based capacitive sensor arrays for object detection at low cost," *Appl. Phys. Lett.*, **92**, 013506, (2008).
- [5] S. P. Beeby *et al.*, "Energy harvesting vibration sources for microsystems applications," *Meas. Sci. Technol.*, **17**, R175, (2006).
- [6] R. Ravichandran *et al.*, "Applications of conducting polymers and their issues in biomedical engineering," *J. Royal Soc. Interface*, rsif20100120, (2010).
- [7] J. Li *et al.*, "Influence of MWCNTs doping on the structure and properties of PEDOT: PSS films," *Int. J. Photoenergy*, **2009**, (2009).
- [8] A. J. Stapleton *et al.*, "Planar silver nanowire, carbon nanotube and PEDOT: PSS nanocomposite transparent electrodes," *Sci. Technol. Adv. Mater.*, **16**, 025002, (2015).
- [9] Y. Park *et al.*, "Efficient flexible organic photovoltaics using silver nanowires and polymer based transparent electrodes," *Org. Electron.*, **36**, 68–72, (2016).

- [10] J. V. Crivello and E. Reichmanis, "Photopolymer materials and processes for advanced technologies," *Chem. Mater.*, **26**, 533–548, (2013).
- [11] H. N. Kim *et al.*, "Patterning methods for polymers in cell and tissue engineering," *Ann. Biomed. Eng.*, **40**, 1339–1355, (2012).
- [12] J. K. Kim *et al.*, "Effect of surface tension and coefficient of thermal expansion in 30 nm scale nanoimprinting with two flexible polymer molds," *Nanotechnology*, **23**, 235303, (2012).
- [13] J. H. Kim *et al.*, "Flexible, stretchable, and patchable organic devices integrated on freestanding polymeric substrates," *J. Polym. Sci., Part B: Polym. Phys.*, **53**, 453–460, (2015).
- [14] K. F. Lei *et al.*, "A flexible PDMS capacitive tactile sensor with adjustable measurement range for plantar pressure measurement," *Microsystem technologies*, **20**, 1351–1358, (2014).
- [15] J. A. Dobrzynska and M. A. M. Gijs, "Polymer–based flexible capacitive sensor for three–axial force measurements," *J. Micromech. Microeng.*, **23**, 015009, (2013).
- [16] S. Yao and Y. Zhu, "Wearable multifunctional sensors using printed stretchable conductors made of silver nanowires," *Nanoscale*, **6**, 2345–2352, (2014).
- [17] H.–K. Kim *et al.*, "Capacitive tactile sensor array for touch screen application," *Sensors and Actuators A: Physical*, **165**, 2–7, (2011).
- [18] H.–K. Lee *et al.*, "A flexible polymer tactile sensor: Fabrication and modular expandability for large area deployment," *J. Microelectromech. Syst.*, **15**, 1681–1686, (2006).
- [19] S. C. B. Mannsfeld *et al.*, "Highly sensitive flexible pressure sensors with microstructured rubber dielectric layers," *Nature materials*, **9**, 859–864, (2010).
- [20] F.–R. Fan *et al.*, "Flexible triboelectric generator," *Nano*

- Energy*, **1**, 328–334, (2012).
- [21] F. Galembeck *et al.*, "Friction, tribochemistry and triboelectricity: recent progress and perspectives," *RSC Adv.*, **4**, 64280–64298, (2014).
- [22] L. S. McCarty and G. M. Whitesides, "Electrostatic charging due to separation of ions at interfaces: contact electrification of ionic electrets," *Angew. Chem. Int. Ed.*, **47**, 2188–2207, (2008).
- [23] S. Niu *et al.*, "Theoretical study of contact–mode triboelectric nanogenerators as an effective power source," *Energy Environ. Sci.*, **6**, 3576–3583, (2013).
- [24] S. Niu *et al.*, "Theory of sliding-mode triboelectric nanogenerators," *Adv. Mater.*, **25**, 6184–6193, (2013).
- [25] N. Sato *et al.*, "Novel surface structure and its fabrication process for MEMS fingerprint sensor," *IEEE Trans. Electron Devices*, **52**, 1026–1032, (2005).
- [26] Y. Zang *et al.*, "Advances of flexible pressure sensors toward artificial intelligence and health care applications," *Materials Horizons*, **2**, 140–156, (2015).
- [27] C. Dagdeviren *et al.*, "Conformable amplified lead zirconate titanate sensors with enhanced piezoelectric response for cutaneous pressure monitoring," *Nature communications*, **5**, 4496, (2014).
- [28] G. Schwartz *et al.*, "Flexible polymer transistors with high pressure sensitivity for application in electronic skin and health monitoring," *Nat. Commun.*, **4**, 1859, (2013).
- [29] B. Zhu *et al.*, "Microstructured graphene arrays for highly sensitive flexible tactile sensors," *Small*, **10**, 3625–3631, (2014).
- [30] C. Pang *et al.*, "A flexible and highly sensitive strain–gauge sensor using reversible interlocking of nanofibres," *Nat. Mater.*, **11**, 795–801, (2012).
- [31] J. Park *et al.*, "Giant tunneling piezoresistance of composite

- elastomers with interlocked microdome arrays for ultrasensitive and multimodal electronic skins," *ACS nano*, **8**, 4689–4697, (2014).
- [32] W. Choi *et al.*, "Enhanced sensitivity of piezoelectric pressure sensor with microstructured polydimethylsiloxane layer," *Appl. Phys. Lett.*, **104**, 123701, (2014).
- [33] M. Akiyama *et al.*, "Flexible piezoelectric pressure sensors using oriented aluminum nitride thin films prepared on polyethylene terephthalate films," *J. Appl. Phys.*, **100**, 114318, (2006).
- [34] J. Chun *et al.*, "Embossed hollow hemisphere-based piezoelectric nanogenerator and highly responsive pressure sensor," *Adv. Funct. Mater.*, **24**, 2038–2043, (2014).
- [35] C.-T. Lee and Y.-S. Chiu, "Piezoelectric ZnO–nanorod–structured pressure sensors using GaN–based field–effect–transistor," *Appl. Phys. Lett.*, **106**, 073502, (2015).
- [36] I. Graz *et al.*, "Flexible active–matrix cells with selectively poled bifunctional polymer–ceramic nanocomposite for pressure and temperature sensing skin," *J. Appl. Phys.*, **106**, 034503, (2009).
- [37] J. Lee *et al.*, "A micro–fabricated force sensor using an all thin film piezoelectric active sensor," *Sensors*, **14**, 22199–22207, (2014).
- [38] J.-J. Wang *et al.*, "Piezoelectric rubber films for highly sensitive impact measurement," *J. Micromech. Microeng.*, **23**, 075009, (2013).
- [39] M. Rahaman *et al.*, "Polyaniline, ethylene vinyl acetate semi-conductive composites as pressure sensitive sensor," *J. Appl. Polym. Sci.*, **128**, 161–168, (2013).
- [40] X. Liu *et al.*, "A highly sensitive pressure sensor using a Au–patterned polydimethylsiloxane membrane for biosensing applications," *J. Micromech. Microeng.*, **23**, 025022, (2013).

- [41] S. Jung *et al.*, "Reverse-micelle-induced porous pressure-sensitive rubber for wearable human-machine interfaces," *Adv. Mater.*, **26**, 4825–4830, (2014).
- [42] S. Chun *et al.*, "A flexible graphene touch sensor in the general human touch range," *Appl. Phys. Lett.*, **105**, 041907, (2014).
- [43] C.-L. Choong *et al.*, "Highly stretchable resistive pressure sensors using a conductive elastomeric composite on a micropylamid array," *Adv. Mater.*, **26**, 3451–3458, (2014).
- [44] B. R. Burg *et al.*, "Piezoresistive pressure sensors with parallel integration of individual single-walled carbon nanotubes," *J. Appl. Phys.*, **109**, 064310, (2011).
- [45] J. Genest *et al.*, "Directly grown large area single-walled carbon nanotube films with very high sensitivity to normal pressure," *J. Appl. Phys.*, **111**, 023502, (2012).
- [46] J.-C. Wang *et al.*, "Characterization of piezoresistive PEDOT:PSS pressure sensors with inter-digitated and cross-point electrode structures," *Sensors*, **15**, 818–831, (2015).
- [47] M.-Y. Cheng *et al.*, "A flexible capacitive tactile sensing array with floating electrodes," *J. Micromech. Microeng.*, **19**, 115001, (2009).
- [48] K. F. Lei *et al.*, "Development of a flexible PDMS capacitive pressure sensor for plantar pressure measurement," *Microelectron. Eng.*, **99**, 1–5, (2012).
- [49] B. Zhang *et al.*, "Dual functional transparent film for proximity and pressure sensing," *Nano Research*, **7**, 1488–1496, (2014).
- [50] X. Wang *et al.*, "Transparent, stretchable, carbon-nanotube-inlaid conductors enabled by standard replication technology for capacitive pressure, strain and touch sensors," *J. Mater. Chem. A*, **1**, 3580–3586, (2013).
- [51] J. Kim *et al.*, "Highly sensitive tactile sensors integrated with organic transistors," *Appl. Phys. Lett.*, **101**, 103308, (2012).

- [52] S.-P. Chang and M. G. Allen, "Demonstration for integrating capacitive pressure sensors with read-out circuitry on stainless steel substrate," *Sens. Actuator A-Phys.*, **116**, 195–204, (2004).
- [53] F. He *et al.*, "A silicon directly bonded capacitive absolute pressure sensor," *Sens. Actuator A-Phys.*, **135**, 507–514, (2007).
- [54] A. D. Kuo, "Harvesting energy by improving the economy of human walking," *Science*, **309**, 1686–1687, (2005).
- [55] S. P. Beeby *et al.*, "Energy harvesting vibration sources for microsystems applications," *Meas. Sci. Technol.*, **17**, R175–R195, (2006).
- [56] P. D. Mitcheson *et al.*, "Energy harvesting from human and machine motion for wireless electronic devices," *Proc. IEEE*, **96**, 1457–1486, (2008).
- [57] Z. L. Wang, "Self-powered nanosensors and nanosystems," *Adv. Mater.*, **24**, 280–285, (2012).
- [58] S. Ju *et al.*, "Fabrication of fully transparent nanowire transistors for transparent and flexible electronics," *Nat. Nanotechnol.*, **2**, 378–384, (2007).
- [59] Y. Yang *et al.*, "Human skin based triboelectric nanogenerators for harvesting biomechanical energy and as self-powered active tactile sensor system," *ACS nano*, **7**, 9213–9222, (2013).
- [60] C. Pang *et al.*, "Flexible transparent and free-standing silicon nanowires paper," *Nano Lett.*, **13**, 4708–4714, (2013).
- [61] H. Li *et al.*, "Novel planar-structure electrochemical devices for highly flexible semitransparent power generation/storage sources," *Nano Lett.*, **13**, 1271–1277, (2013).
- [62] K. Y. Lee *et al.*, "Transparent flexible stretchable piezoelectric and triboelectric nanogenerators for powering portable electronics," *Nano Energy*, **14**, 139–160, (2015).

- [63] N. Li *et al.*, "Free-standing and transparent graphene membrane of polyhedron box-shaped basic building units directly grown using a NaCl template for flexible transparent and stretchable solid-state supercapacitors," *Nano Lett.*, **15**, 3195–3203, (2015).
- [64] G. Zhu *et al.*, "Trieoelectric nanogenerators as a new energy technology: from fundamentals, devices, to applications," *Nano Energy*, **14**, 126–138, (2015).
- [65] S. Niu and Z. L. Wang, "Theoretical systems of trieoelectric nanogenerators," *Nano Energy*, **14**, 161–192, (2015).
- [66] Z. Wang *et al.*, "Enhancing the performance of trieoelectric nanogenerator through prior-charge injection and its application on self-powered anticorrosion," *Nano Energy*, **10**, 37–43, (2014).
- [67] S. Wang *et al.*, "Nanoscale trieoelectric-effect-enabled energy conversion for sustainably powering portable electronics," *Nano Lett.*, **12**, 6339–6346, (2012).
- [68] G. Zhu *et al.*, "Toward large-scale energy harvesting by a nanoparticle-enhanced trieoelectric nanogenerator," *Nano Lett.*, **13**, 847–853, (2013).
- [69] C. K. Jeong *et al.*, "Topographically-designed trieoelectric nanogenerator via block copolymer self-assembly," *Nano Lett.*, **14**, 7031–7038, (2014).
- [70] M.-L. Seol *et al.*, "Nature-replicated nano-in-micro structures for trieoelectric energy harvesting," *Small*, **10**, 3887–3894, (2014).
- [71] J. Chen *et al.*, "Harmonic-resonator-based trieoelectric nanogenerator as a sustainable power source and a self-powered active vibration sensor," *Adv. Mater.*, **25**, 6094–6099, (2013).
- [72] S. Kim *et al.*, "Transparent flexible graphene trieoelectric nanogenerators," *Adv. Mater.*, **26**, 3918–3925, (2014).
- [73] G. Zhu *et al.*, "Self-powered, ultrasensitive, flexible tactile

- sensors based on contact electrification," *Nano Lett.*, **14**, 3208–3213, (2014).
- [74] F. Yi *et al.*, "Self-powered trajectory, velocity, and acceleration tracking of a moving object/body using a triboelectric sensor," *Adv. Funct. Mater.*, **24**, 7488–7494, (2014).
- [75] J. Chun *et al.*, "Mesoporous pores impregnated with Au nanoparticles as effective dielectrics for enhancing triboelectric nanogenerator performance in harsh environments," *Energy Environ. Sci.*, **8**, 3006–3012, (2015).
- [76] K. Y. Lee *et al.*, "Fully Packaged Self-Powered Triboelectric Pressure Sensor Using Hemispheres-Array," *Adv. Energy Mater.*, **6**, 1502566, (2016).
- [77] S.-J. Park *et al.*, "Surface engineering of triboelectric nanogenerator with an electrodeposited gold nanoflower structure," *Sci. Rep.*, **5**, 13866, (2015).
- [78] D. Jang *et al.*, "Force-assembled triboelectric nanogenerator with high-humidity-resistant electricity generation using hierarchical surface morphology," *Nano Energy*, **20**, 283–293, (2016).
- [79] C. J. Lee *et al.*, "Triboelectric generator for wearable devices fabricated using a casting method," *RSC Adv.*, **6**, 10094–10098, (2016).
- [80] L. Dhakar *et al.*, "Large scale triboelectric nanogenerator and self-powered pressure sensor array using low cost roll-to-roll UV embossing," *Sci. Rep.*, **6**, 22253, (2016).
- [81] X. Cheng *et al.*, "Single-step fluorocarbon plasma treatment-induced wrinkle structure for high-performance triboelectric nanogenerator," *Small*, **12**, 229–236, (2016).
- [82] F.-R. Fan *et al.*, "Transparent triboelectric nanogenerators and self-powered pressure sensors based on micropatterned plastic films," *Nano Lett.*, **12**, 3109–3114, (2012).

- [83] F. R. Fan *et al.*, "Highly transparent and flexible triboelectric nanogenerators: performance improvements and fundamental mechanisms," *J. Mater. Chem. A*, **2**, 13219–13225, (2014).
- [84] B. Dudem *et al.*, "Highly transparent and flexible triboelectric nanogenerators with subwavelength-architected polydimethylsiloxane by a nanoporous anodic aluminum oxide template," *ACS Appl. Mater. Interfaces*, **7**, 20520–20529, (2015).
- [85] X. He *et al.*, "Flexible and transparent triboelectric nanogenerator based on high performance well-ordered porous PDMS dielectric film," *Nano Res.*, **9**, 3714–3724, (2016).
- [86] A. I. Uddin *et al.*, "Improving the working efficiency of a triboelectric nanogenerator by the semimetallic PEDOT: PSS hole transport layer and its application in self-powered active acetylene gas sensing," *ACS Appl. Mater. Interfaces*, **8**, 30079–30089, (2016).
- [87] Y. Kim *et al.*, "PEDOT as a flexible organic electrode for a thin film acoustic energy harvester," *ACS Appl. Mater. Interfaces*, **7**, 16279–16286, (2015).
- [88] A. Šutka *et al.*, "PEDOT electrodes for triboelectric generator devices," *Org. Electron.*, **51**, 446–451, (2017).
- [89] J. Yang *et al.*, "Surface engineering of graphene composite transparent electrodes for high performance flexible triboelectric nanogenerators and self-powered sensors," *ACS Appl. Mater. Interfaces*, **9**, 36017–36025, (2017).
- [90] J. Ouyang *et al.*, "On the mechanism of conductivity enhancement in poly (3, 4-ethylenedioxythiophene): poly (styrene sulfonate) film through solvent treatment," *Polymer*, **45**, 8443–8450, (2004).
- [91] M. Vosgueritchian *et al.*, "Highly conductive and transparent PEDOT: PSS films with a fluorosurfactant for stretchable and flexible transparent electrodes," *Adv. Funct. Mater.*, **22**, 421–428, (2012).

- [92] B.-Y. Lee *et al.*, "Low-cost flexible pressure sensor based on dielectric elastomer film with micro-pores," *Sensors and Actuators A: Physical*, **240**, 103–109, (2016).
- [93] H. Kang *et al.*, "Mechanically robust silver nanowires network for triboelectric nanogenerators," *Adv. Funct. Mater.*, **26**, 7717–7724, (2016).
- [94] K.-E. Byun *et al.*, "Control of triboelectrification by engineering surface dipole and surface electronic state," *ACS Appl. Mater. Interfaces*, **8**, 18519–18525, (2016).
- [95] H. Peng and X. Sun, "Highly aligned carbon nanotube/polymer composites with much improved electrical conductivities," *Chem. Phys. Lett.*, **471**, 103–105, (2009).
- [96] R. H. Baughman *et al.*, "Carbon nanotubes—the route toward applications," *Science*, **297**, 787–792, (2002).
- [97] G.-G. Cheng *et al.*, "Effect of argon plasma treatment on the output performance of triboelectric nanogenerator," *Appl. Surf. Sci.*, **412**, 350–356, (2017).
- [98] X. Wang *et al.*, "Self-powered high-resolution and pressure-sensitive triboelectric sensor matrix for real-time tactile mapping," *Adv. Mater.*, **28**, 2896–2903, (2016).

Publications

International Journals

- [1] S.-U. Kim, **B.-Y. Lee**, J.-H. Suh, J. Kim, J.-H. Na, S.-D. Lee, “Reduction of gamma distortions in liquid crystal display by anisotropic voltage-dividing layer of reactive mesogens”, *Liq. Cryst.*, **44**, 364 (2016)
- [2] **B.-Y. Lee**, J. Kim, H. Kim, C. Kim, S.-D. Lee, “Low-cost flexible pressure sensor based on dielectric elastomer film with micro-pores”, *Sens. Actuators A-Phys.*, **240**, 103 (2016)
- [3] H.-L. Park, **B.-Y. Lee**, S.-U. Kim, J.-H. Suh, M.-H. Kim, S.-D. Lee, “Importance of surface modification of a microcontact stamp for pattern fidelity of soluble organic semiconductors”, *J. Micro Nanolithogr. MEMS MOEMS*, **15**, 013501 (2016)
- [4] J. Kim, S.-U. Kim, **B.-Y. Lee**, J.-H. Suh, S.-D. Lee, “Lenticular lens array based on liquid crystal with a polarization-dependent focusing effect for 2D-3D image applications”, *J. Inf. Disp.*, **16**, 11 (2015)
- [5] S.-U. Kim, J. Kim, E.-S. Yu, I.-H. Lee, **B.-Y. Lee**, Y. Sohn, S.-D. Lee, “Colloidal assembling template with wrinkled patterns based on liquid crystalline polymer”, *Mol. Cryst. Liq. Cryst.*, **610**, 221 (2015)
- [6] J. Kim, J.-H. Suh, **B.-Y. Lee**, S.-U. Kim, S.-D. Lee, “Optically switchable grating based on dye-doped ferroelectric liquid crystal with high efficiency” *Opt. Express*, **23**, 12619 (2015)

International Conferences

- [1] **B.-Y. Lee**, S. Kang, S.-D. Lee, “Effect of the surface potential and the conductivity of a conducting polymer on flexible triboelectric nanogenerators”, *The 4th International Conference on Advanced Electromaterials*, Jeju, Korea (2017)
- [2] **B.-Y. Lee**, S.-U. Kim, S. Kang, C. Kim, S.-D. Lee, “All-organic triboelectric nanogenerators for highly efficient, transparent and flexible power sources”, *The 17th International Meeting on Information Display*, Busan, Korea (2017)
- [3] S. Kang, **B.-Y. Lee**, J.-H. Suh, C. Kim, S.-D. Lee, “Solvent effect on emission properties of solution-processed organic light-emitting diodes”, *The 28th International Conference on Molecular Electronics and Devices*, Seoul, Korea (2017)
- [4] S. Kang, J.-H. Suh, **B.-Y. Lee**, C. Kim, S.-D. Lee, “Optical micro-resonators based on reactive-mesogen doped with quantum-dots for color elements”, *The 6th Symposium on Liquid Crystal Photonics*, Tianjin, China (2017)
- [5] **B.-Y. Lee**, S. Kang, S.-D. Lee, “Transparent and flexible triboelectric nanogenerators based on nano wire-polymer composite”, *International Workshop on Flexible & Printable Electronics*, Jeonju, Korea (2016)
- [6] G. Lee, I.-H. Lee, H.-L. Park, S.-H. Lee, E.-S. Yu, **B.-Y. Lee**, S.-D. Lee, “Effect of injection barrier height on current on/off ratio of vertical organic-field-effect transistor”, *The 16th International Meeting on Information Display*, Jeju, Korea (2016)
- [7] S. Kang, **B.-Y. Lee**, S.-D. Lee, “High-fidelity patterning of conducting polymers on stretchable substrate using selective wetting technique”, *The 16th International Meeting on Information Display*, Jeju, Korea (2016)
- [8] H. Kim, H.-L. Park, S.-U. Kim, J.-H. Suh, **B.-Y. Lee**, S.-D. Lee, “Construction of high-fidelity patterns of solution-processed organic light-emitting diodes using surface modified banks by wettability”, *The 16th International Meeting on Information Display*, Jeju, Korea (2016)

- Display*, Jeju, Korea (2016)
- [9] G. Lee, I.-H. Lee, H.-L. Park, **B.-Y. Lee**, S.-H. Lee, E.-S. Yu, J. Han, C. Lee, S.-D. Lee, “Encapsulation effect of source electrode on gate-voltage controllability in vertical organic light-emitting transistors”, *International Conference on Organic Electronics*, Bratislava, Slovakia (2016)
- [10] **B.-Y. Lee**, I.-H. Lee, S.-U. Kim, S.-D. Lee, “Tribocharge transfer mechanism in conducting polymer-based triboelectric nanogenerators for transparent and flexible energy harvesting devices”, *International Conference on Organic Electronics*, Bratislava, Slovakia (2016)
- [11] S.-U. Kim, **B.-Y. Lee**, J.-H. Suh, J. Kim, S.-D. Lee, “Voltage-division technique by reactive mesogen layer for gamma-distortion reduction in liquid crystal displays”, *The 5th Symposium on Liquid Crystal Photonics*, Beijing, China (2016)
- [12] S.-U. Kim, J. Kim, J.-H. Suh, **B.-Y. Lee**, S.-D. Lee, “New vertical alignment mode of liquid crystal display with reduced gamma distortions by periodic patterns of reactive mesogens on alignment layer”, *The 15th International Meeting on Information Display*, Daegu, Korea (2015)
- [13] **B.-Y. Lee**, J. Kim, S.-D. Lee, “Flexible pressure sensor array based on highly elastic porous film”, *The 15th International Meeting on Information Display*, Daegu, Korea (2015)
- [14] H.-L. Park, **B.-Y. Lee**, C.-M. Keum, S.-U. Kim, M.-H. Kim, S.-D. Lee, “Improvement of micro-contact patterning fidelity of organic semiconductors through ultraviolet ozone treatment on nanoporous stamps”, *Society of Photographic Instrumentation Engineers Optics + Photonics*, San Diego, USA (2015)
- [15] S.-D. Lee, J. Kim, S.-U. Kim, **B.-Y. Lee**, J.-H. Suh, “Realization of 2D/3D switchable displays with tunable lens array”, *The 4th Symposium on Liquid Crystal Photonics*, Shenzhen, China (2015)
- [16] J.-H. Suh, **B.-Y. Lee**, J. Kim, S.-U. Kim, S.-D. Lee, “Wide-

range control of liquid crystal anchoring energy based on siloxane oligomer transfer”, *The 2nd Asian Conference on Liquid Crystals*, Busan, Seoul (2015)

- [17] J. Kim, S.-U. Kim, **B.-Y. Lee**, J.-H. Suh, S.-D. Lee, “Imprinted lenticular lens array based on liquid crystal for autostereoscopic 2D/3D switchable displays”, *The 14rd International Meeting on Information Display*, Daegu, Korea (2014)
- [18] S.-U. Kim, J. Kim, E.-S. Yu, I.-H. Lee, **B.-Y. Lee**, S.-D. Lee, “Multi-directional colloidal assembly on wrinkled liquid crystalline polymer template”, *25th International Liquid Crystal Conference*, Dublin, Ireland (2014)
- [19] H.-L. Park, C.-M. Keum, **B.-Y. Lee**, S.-H. Lee, S.-D. Lee, “Engineering the work function of inkjet-printed electrodes in all-solution-processed organic field-effect transistors”, *European Materials Research Society*, Lille, France (2014)
- [20] **B.-Y. Lee**, J. Kim, S.-U. Kim, S.-D. Lee, “Capacitive pressure sensor based on porous hydrophobic elastomer for flexible electronic applications”, *European Materials Research Society*, Lille, France (2014)
- [21] J. Kim, S.-U. Kim, **B.-Y. Lee**, S.-D. Lee, “Electrically switchable square lens array based on liquid crystals”, *Optics of Liquid Crystals 2013*, Hawaii, USA (2013)
- [22] **B.-Y. Lee**, S. C. Park, M.-H. Kim, J. Kim, S.-D. Lee, “Highly pressure-sensitive capacitive sensors based on porous elastomers for touch panel applications”, *The 13rd International Meeting on Information Display*, Daegu, Korea (2013)
- [23] J. Kim, S.-U. Kim, **B.-Y. Lee**, S.-D. Lee, “Liquid crystal-based hybrid optical retarder varying a quarter-to-half wave for three-dimensional displays”, *The 13rd International Meeting on Information Display*, Daegu, Korea (2013)

국문초록

최근 사물인터넷 시대의 도래와 함께 다양한 웨어러블 소자에 대한 관심이 급증하고 있다. 기존 전자소자와는 달리 웨어러블 소자는 휴대하기 용이해야 하며 더 나아가 신체에 부착할 수 있도록 유연한 소재의 가벼운 박막형을 추구한다. 또한, 웨어러블 전자소자의 진정한 상용화를 위해서는 사용자와 우호적 상호작용을 가능하게 하는 감지기술 구현과 기존의 배터리가 가지고 있는 사용시간의 제한적 문제와 부피 크기에 대한 문제를 해결할 수 있는 새로운 전력 시스템 구축에 대한 연구가 필수적이다. 본 논문은 고성능 웨어러블 소자 응용에 적합한 압력센서와 에너지 하베스팅 소자를 제안하며 고감도의 정전용량 식 유연압력센서 및 고효율의 투명하고 유연한 에너지 하베스팅 소자에 초점을 맞춘다.

먼저, 감지 기술 중에서 압력감지기술은 단순히 접촉여부를 판단하는 수준을 넘어서서 접촉의 강도를 구분할 수 있기 때문에 터치패널로의 응용뿐 아니라 건강 모니터링 시스템 등 각종 차세대 전자기기에 폭넓게 적용될 수 있다. 특히 고감도 유연압력센서는 사람의 움직임보다 정확하게 감지하거나 더 나아가 사람의 피부를 모사할 수 있기 때문에 그 기술의 중요성이 더욱 부각되고 있다. 그러나, 기존 기술들은 낮은 민감도를 보이거나 복잡하고 값비싼 공정이 요구되어 실질적인 응용에는 한계를 지니고 있었다. 따라서 본 논문에서는 유연압력센서의 민감도를 향상시킬 수 있는 핵심소재를 간단하고 비용효율이 높은 공정기술 도입을 통해 개발하고, 이 소재가 적용된 유연센서를 제안한다. 균일한 미세 기공을 통해 탄성체 필름의 탄성력을

향상시켜 같은 압력에도 큰 변형을 유도하였다. 개발된 유연압력센서는 피부의 감도와 유사한 낮은 압력에서도 높은 민감도와 빠른 반응속도를 보인다.

다음으로, 에너지 하베스팅 기술은 지속적이고 독립적인 전원공급이 가능하다는 점에서 많은 관심을 받아왔다. 특히 주변의 기계적 움직임을 전기로 사용할 수 있는 마찰전기 나노발전기는 물질사용에 대한 제한이 적어 가볍고 유연한 형태로 제작 가능할 뿐만 아니라 기존에 자주 사용되는 압전 방식에 비해 높은 출력성능을 보여 활발한 연구가 이루어지고 있다. 그러나, 이 금속 층의 필수적 사용으로 인해 유연한 소자 구현이 어렵다는 단점을 지니고 있다. 이를 해결하기 위해 금속을 유연전극으로 대체하는 연구들이 제안되었지만, 이들은 낮은 전력밀도의 한계를 지니고 있었다. 본 논문에서는 나노 구조물이 도입된 전도성 고분자 층을 활용한 고성능 마찰전기발전기에 대해 기술한다. 전도성 고분자는 전자전도도가 높아 마찰전기발전기의 성능 향상에 기여할 뿐만 아니라 높은 투명도 및 유연성을 지니고 있어 웨어러블 소자로의 응용에 적합하다. 뿐만 아니라 은나노와이어의 도입을 통해 전도성 고분자 층의 전도성과 표면적을 증대시켜 출력성능을 더욱 증가시킬 수 있었다. 본 논문에서 제안된 소자는 기존의 투명하고 유연한 마찰전기발전기에 비해 높은 출력성능을 보인다.

요약하자면, 미세구조가 도입된 탄성층이나 전도성고분자 및 나노와이어 복합체층과 같은 나노구조물의 기능성고분자를 활용하여 웨어러블 소자의 핵심기술인 압력센서와 마찰전기발전기의 성능을 향상시키는 데에 주력하였다. 본 논문에서 제안된 방법들은 향후 고성능 웨어러블 소자로의 응용 연구에 큰 기여를 할 것으로 기대된다.

주요 용어: 웨어러블 전자소자, 고분자 나노 복합체, 탄성체, 유연센서, 정전용량식 압력센서, 마찰전기 나노발전기

학번: 2012-20834